

## Research papers



# Three-dimensional experimental-scale phase-field modeling of dendrite formation in rechargeable lithium-metal batteries

Marcos E. Arguello<sup>a,b,\*</sup>, Nicolás A. Labanda<sup>c,d</sup>, Victor M. Calo<sup>c</sup>, Monica Gumulya<sup>e</sup>, Ranjeet Utikar<sup>a</sup>, Jos Derksen<sup>b</sup>

<sup>a</sup> WA School of Mines, Mineral, Energy and Chemical Engineering, Curtin University, P.O. BOX U1987, Perth, WA 6845, Australia

<sup>b</sup> School of Engineering, University of Aberdeen, Elphinstone Road, AB24 3UE Aberdeen, United Kingdom

<sup>c</sup> School of Electrical Engineering, Computing and Mathematical Sciences, Curtin University, P.O. Box U1987, Perth, WA 6845, Australia

<sup>d</sup> SRK Consulting, West Perth, Western Australia, Australia

<sup>e</sup> Occupation, Environment and Safety, School of Population Health, Curtin University, P.O. Box U1987, Perth, WA 6845, Australia

## ARTICLE INFO

## Keywords:

Phase-field modeling  
Lithium dendrite  
Inter-electrode distance  
Surface anisotropy  
Metal-anode battery  
Finite element method

## ABSTRACT

This paper presents a phase-field based numerical study on the 3D formation of dendrites due to electrodeposition in an experimental-scale lithium metal battery. Small-scale 3D simulations were firstly conducted to elucidate the characteristics and resolution requirements of the numerical framework. Using a four-fold anisotropy model to simulate the growth of lithium deposition, the dependency of dendrite morphology on charging conditions ( $\phi_b = -0.7[V]$  and  $\phi_b = -1.4[V]$ ) on a (larger) experimental-scale metal anode was demonstrated. The dendrite shape was found to shift from a smoother, tree-like formation at the lower applied voltage, to a more spike-like, highly branched structure at the higher voltage. The resulting morphological parameters, such as dendrite propagation rates, volume-specific area, and side branching rates, were compared against published experimental data and found to be comparable to the reported ranges for the electrodeposition of spike- or tree-like metal dendrites. This finding supports our previous observation that dendrite formation is connected to the competition between the lithium cation diffusion and electric migration, generating an uneven distribution of  $\text{Li}^+$  on the electrode surface. This observation also gives insight into dendrite inhibition strategies focusing on enhancing the diffusion of lithium ions to achieve a more uniform concentration field on the anode surface.

## 1. Introduction

Global energy demand continues to rise due to industrial activity and the world's population expansion, with an average growth rate of about 1% to 2% per year since 2010 (pre-Covid19 pandemic levels) [1]. The increasing consumption of non-renewable energy reserves, such as coal, gas, and oil [2], and awareness of climate change [3,4], have triggered a steep growth in renewable energy sources (6% average annual growth worldwide over the past decade) [5], along with an urgent need for the development of improved energy storage systems [6]. Globally, around one-quarter of our electricity comes from renewables, which include hydropower, wind, solar, biomass, ocean energy, biofuel, and geothermal [1].

New chemistry and designs, such as metal anode batteries, are under active research to achieve a specific energy of 500 Wh/kg and manufacturing costs lower than \$100/kWh [7]. Despite enormous efforts, today's highest specific energy remains below 400 Wh/kg, with

an average growth rate of about 5% per year since 1970 [8]. As the specific energy limitation (300 Wh/kg) of conventional lithium-ion batteries based on intercalated graphite anode cannot meet the current market demand, researchers are refocusing on lithium metal batteries (LMBs) [9]. LMBs can achieve ultra-high energy densities by avoiding the use of a graphite lattice to host  $\text{Li}^+$  (intercalation process), as illustrated by the comparative schematic of Fig. 1. The graphite material (host) drastically reduces the energy density of conventional Li-ion batteries by adding weight to the battery pack that does not participate in the electrochemical reaction [8]. For instance, a recent study by Mathieu et al. [10] analyzed the key materials that make up battery cells for medium-sized electric vehicles (weighted average of the battery chemistries commercialized in 2020 [10]). This study revealed that graphite material (anode) represented the largest share, accounting for 28% of the total weight of the battery cell. Furthermore, according to Lin et al. [11], the specific energy delivered by state-of-the-art Li-ion cells (250 Wh/kg) can be increased to approximately 440

\* Corresponding author at: WA School of Mines, Mineral, Energy and Chemical Engineering, Curtin University, P.O. BOX U1987, Perth, WA 6845, Australia.

E-mail addresses: [m.arguello@postgrad.curtin.edu.au](mailto:m.arguello@postgrad.curtin.edu.au), [m.arguello.19@abdn.ac.uk](mailto:m.arguello.19@abdn.ac.uk) (M.E. Arguello), [nlabanda@srk.com.au](mailto:nlabanda@srk.com.au) (N.A. Labanda), [victor.calo@curtin.edu.au](mailto:victor.calo@curtin.edu.au) (V.M. Calo), [m.gumulya@curtin.edu.au](mailto:m.gumulya@curtin.edu.au) (M. Gumulya), [r.utikar@curtin.edu.au](mailto:r.utikar@curtin.edu.au) (R. Utikar), [jderksen@abdn.ac.uk](mailto:jderksen@abdn.ac.uk) (J. Derksen).

<https://doi.org/10.1016/j.est.2023.106854>

Received 7 November 2022; Received in revised form 10 January 2023; Accepted 6 February 2023

2352-152X/© 2023 Elsevier Ltd. All rights reserved.

**Nomenclature**

$A^-$	Anion species [-]
$C_m^l$	Site density electrolyte [mol/m <sup>3</sup> ]
$C_m^s$	Site density electrode [mol/m <sup>3</sup> ]
$C_0$	Bulk Li-ion concentration [mol/m <sup>3</sup> ]
$D^{eff}$	Effective diffusivity [m <sup>2</sup> /s]
$\vec{E}$	Electric field vector [V/m]
$E_0$	Energy density normalization constant [J/m <sup>3</sup> ]
$F$	Faraday constant [s A/mol]
$f_{ch}$	Helmholtz free energy density [J/m <sup>3</sup> ]
$f_{grad}$	Surface energy density [J/m <sup>3</sup> ]
$f_{elec}$	Electrostatic energy density [J/m <sup>3</sup> ]
$g(\xi)$	Double-well function [J/m <sup>3</sup> ]
$h$	Mesh size [m]
$H$	Dendrite height [m]
$h(\xi)$	Interpolation function [-]
$h_0$	Length normalization constant [m]
$i$	Current density [A/m <sup>2</sup> ]
$i_0$	Exchange current density [A/m <sup>2</sup> ]
$L_\eta$	Kinetic coefficient [1/s]
$L_\sigma$	Interfacial mobility [m <sup>3</sup> /(J s)]
$l_x$	Longitudinal battery cell size (x direction) [m]
$l_{x_u}$	Region of interest [m]
$l_y$	Lateral battery cell size (y direction) [m]
$l_z$	Lateral battery cell size (z direction) [m]
$M$	Metal atom species [-]
$M^+$	Cation species [-]
$n$	Valence [-]
$R$	Gas constant [J/(mol K)]
$\mathcal{R}$	Phase-field interface thickness to mesh resolution ratio [-]
$T$	Temperature [K]
$t$	Time [s]
$t_0$	Time normalization constant [s]
$W$	Barrier height [J/m <sup>3</sup> ]
$\alpha$	Charge transfer coefficient [-]
$\gamma$	Surface Energy [J/m <sup>2</sup> ]
$\delta_{aniso}$	Anisotropy strength [-]
$\delta_{PF}$	Phase-field diffuse interface thickness [m]
$\tilde{c}_+$	Normalized Li-ion concentration [-]
$\eta$	Total overpotential [V]
$\kappa$	Gradient energy coefficient variable [J/m]
$\kappa_0$	Gradient energy coefficient constant [J/m]
$\xi$	Phase-field order parameter [-]
$\sigma^{eff}$	Effective conductivity [S/m]
$\phi$	Electric potential [V]

$\phi_b$	Charging voltage [V]
$\Psi$	Gibbs free energy [J]
$\omega$	Anisotropy mode [-]

to achieving the commercial realization of lithium-metal batteries is related to their stability and safety [11]. These issues are closely linked to the lithium anode: dendrite formation due to the uneven deposition of lithium, dead lithium formed after dendrites breakage, formation of unstable solid electrolyte interphase (SEI), and volume expansion of the metal anode. Additionally, these mechanisms interact, causing synergistic detrimental effects [12].

Dendrite formation in LMBs is the consequence of lithium's uneven deposition, associated with thermodynamic and kinetic factors, such as the inhomogeneous distribution of Li-ion concentration and electric potential on the electrode surface. Furthermore, the morphology of the electrodeposited lithium is influenced by different factors such as the magnitude and frequency of the applied current density, electrolyte concentration, temperature, pressure, ion transport, and mechanical properties in the electrolyte [13,14]. Understanding dendrite formation in LMBs combines theory, experiment, and computation [15]. Within computational research, various studies have demonstrated the use of phase-field (diffuse-interface) method to model the reaction-driven phase transformation within metal anode batteries, providing avenues for rationalization of morphological behaviors of dendrite formations observed experimentally [16–45].

While progress has occurred in phase-field modeling of lithium dendrites in recent years, there are still several issues related to the evolution of dendritic patterns in lithium metal electrodes that remain unresolved [38]. The fundamental failure mechanism of lithium anode remains unclear and controversial [12]. A significant effort has gone into using 2D models to rationalize 3D dendritic patterns observed experimentally [43]. Furthermore, various strategies exist to suppress Li dendrites' growth and weaken side reactions. Some of these strategies address the battery operating conditions, including pulse charging lithium dendrite suppression [41] and control of internal temperature [28]. Other alternatives focus on the electrode (anode), such as modeling of 3D conductive structured lithium metal anode [33,44], and low porosity and stable SEI structure [30]. Besides, other approaches center on the electrolyte management and separator design, proposing a compositionally graded electrolyte [27], dendrite suppression using flow field (forced advection) [32], the study of separator pore size inhibition effect on lithium dendrite [45].

Given the inherent 3D nature of lithium dendrite morphologies [31, 46,47], it is critical to develop phase-field models to understand the impact of 3D effects on triggering the formation of these patterns. Nevertheless, few papers attempt to simulate the full 3D lithium dendrite growth process using phase-field models. For instance, Mu et al. [37] performed parallel three-dimensional phase-field simulations of dendritic lithium evolution under different electrochemical states, including charging, suspending, and discharging states. Recently, Arguello et al. [43] presented 3D phase-field simulations using an open-source finite element library, to describe hazardous three-dimensional dendritic patterns in LMBs. The authors used time step adaptivity, mesh rationalization, parallel computation, and balanced phase-field interface thickness to mesh resolution ratio. The high computational cost of simulating the detailed lithium electrodeposition is a well-known challenge that has limited the domain size of phase-field simulations [26, 29]. Thus, higher-than-normal dendrite growth rates were reported in the literature for 3D phase-field modeling of dendrite growth, due to the short separation between electrodes used [37,43]. Recently, experimental observations by Chae et al. [48] have revealed a change in the lithium deposition behavior and morphology from "hazardous" needle- and moss-like dendritic structures to "safer" morphologies

Wh/kg once the graphite anode is replaced by lithium in a Li-LMO cell (lithium transition-metal oxide).

Although lithium metal has been an attractive anode alternative in rechargeable batteries since the early 1970s, its commercialization has been hindered due to several shortcomings. The greatest challenge

(smooth and round shaped surface) as interelectrode spacing increases. Therefore, simulating the dendrite formation at the experimental scale has significant practical relevance.

In this paper, we seek to present a 3D phase-field model of lithium dendrite formation in an experimental scale battery. The domain sizes simulated here (with up-to 5000 [μm] inter-electrode separation) represent a significant extension towards practical application compared to previous 3D phase-field electrodeposition works, where separations of only about 100 [μm] could be achieved due to computational cost limitation [37,43].

Here we expand on our previous work on the phase-field model [42, 43]; we use small-scale 3D simulations to analyze the sensitivity of the model on spatial resolution and phase-field interface thickness to determine the numerical requirements of the experimental scale simulations.

We also look into the incorporation of a modified 3D representation of the surface anisotropy based on the cubic crystal structure of lithium [29], as well as the model of William et al. [49]. Besides the 2D work by Wang et al. [50] on dendrite formation in zinc-air batteries, our work presents the application of the corresponding surface anisotropy approach in a 3D phase-field model of dendrite electrodeposition for the first time in the literature.

We organize the paper as follows: Section 2 presents the basic equations describing the lithium-battery dendrite growth process and details its implementation where we introduce a modified representation of the surface anisotropy of lithium metal. Section 3 describes the system layout and properties, together with the implementation of symmetric boundary conditions for a detailed study of symmetric dendritic patterns [31,47]. We discuss numerical simulations of spike-like (small scale) lithium-battery dendrites growth in Section 4, where we analyze the sensitivity of the simulation results for a series of spatial resolutions and phase-field interface thickness. Section 5 evaluates the behavior of the surface anisotropy representation model for metal anode battery simulations through different numerical tests. We compare the dendritic patterns with the results obtained in preceding simulation work [43]. Following this, we present our implementation of the modified surface anisotropy model under a larger interelectrode distance (experimental scale) 6. We show that a significant modification in lithium electrodeposition behavior is obtained with increasing interelectrode distance. We study and describe the lithium dendrite propagation rates and morphologies obtained under different charging voltages. Finally, we draw conclusions in Section 7.

## 2. Formulation & implementation

### 2.1. Surface anisotropy representation for phase-field electrodeposition models

In this section, we present a modified representation of the 3D surface anisotropy of crystalline lithium. We start by considering the surface energy expression, following [42,43]:  $f_{\text{grad}} = \frac{1}{2}\kappa(\xi)(\nabla\xi)^2$ , where its variational derivative (surface anisotropy of lithium crystal) is:  $\frac{\delta f_{\text{grad}}}{\delta\xi} = \kappa(\xi)\nabla^2\xi$ , consistent with most recent phase-field models of dendritic electrodeposition [24–27,30,38]. However, a more accurate representation of  $\frac{\delta f_{\text{grad}}}{\delta\xi}$  may include an additional term, as originally derived by Kobayashi [51] for 2D crystal growth. In 3D, we use the variational derivative version derived by George & Warren [49] to simulate the surface anisotropy of crystal growth

$$\frac{\delta f_{\text{grad}}}{\delta\xi} = \frac{\delta}{\delta\xi} \left[ \frac{1}{2}a^2(\nabla\xi)^2 \right] = \nabla \cdot (a^2\nabla\xi) + \sum_{i=1}^3 \frac{\partial}{\partial x_i} \left[ a \frac{\partial a}{\partial \left( \frac{\partial\xi}{\partial x_i} \right)} (\nabla\xi)^2 \right], \quad (1)$$

where  $a^2 = \kappa(\xi)$  is the three-dimensional surface anisotropy or gradient coefficient. The first term after the last equality remains the same

as in the previous surface anisotropy expression; however, we add a second term (derivation due to  $\kappa$  as a function of  $\xi$ ). We calculate the partial derivative  $\frac{\partial a}{\partial \left( \frac{\partial\xi}{\partial x_i} \right)}$  in (1). We express the 3D surface anisotropy coefficient (four-fold anisotropy) [43,49], as:

$$a(\xi) = \sqrt{\kappa_0} (1 - 3\delta_{\text{aniso}}) \left[ 1 + \frac{4\delta_{\text{aniso}}}{1 - 3\delta_{\text{aniso}}} \left( \frac{\sum_{i=1}^3 \left( \frac{\partial\xi}{\partial x_i} \right)^4}{\|\nabla\xi\|^4} \right) \right], \quad (2)$$

where  $x_1 = x$ ,  $x_2 = y$ , and  $x_3 = z$ ;  $\kappa_0$  relates to the Lithium surface tension  $\gamma$ ; and  $\delta_{\text{aniso}}$  is the strength of anisotropy [52,53]. Thus, we apply the quotient derivative rule to (2) and arrive at the partial derivative expression we use in (1); subsequently:

$$\begin{aligned} \frac{\partial a}{\partial \left( \frac{\partial\xi}{\partial x_i} \right)} &= 4\sqrt{\kappa_0}\delta_{\text{aniso}} \left[ \frac{4 \left( \frac{\partial\xi}{\partial x_i} \right)^3 \|\nabla\xi\|^4 - \left( \frac{\partial\xi}{\partial x_i} \right)^4 4\|\nabla\xi\|^3 \frac{\partial\|\nabla\xi\|}{\partial \left( \frac{\partial\xi}{\partial x_i} \right)}}{\|\nabla\xi\|^8} \right] \\ &= 4\sqrt{\kappa_0}\delta_{\text{aniso}} \left[ \frac{4 \left( \frac{\partial\xi}{\partial x_i} \right)^3 \|\nabla\xi\|^4 - 4 \left( \frac{\partial\xi}{\partial x_i} \right)^4 \|\nabla\xi\|^3 \frac{\partial\xi}{\partial x_i}}{\|\nabla\xi\|^8} \right] \\ &= 4\sqrt{\kappa_0}\delta_{\text{aniso}} \left[ \frac{4 \left( \frac{\partial\xi}{\partial x_i} \right)^3 \|\nabla\xi\|^2 - 4 \left( \frac{\partial\xi}{\partial x_i} \right)^5}{\|\nabla\xi\|^6} \right] \\ &= 4\sqrt{\kappa_0}\delta_{\text{aniso}} \left[ \frac{4(n_i^3 - n_i^5)}{\|\nabla\xi\|} \right] \text{ for } i = 1, 2, 3, \end{aligned} \quad (3)$$

where  $n_i = \frac{\partial\xi}{\partial x_i} \frac{\partial\xi}{\|\nabla\xi\|}$  for  $i = 1, 2, 3$ .

Although its extensive use in phase-field models of crystal growth (solidification) [49,54], only Wang et al. [50] apply these models to a 2D phase-field simulation of dendrite growth in the recharging process of zinc-air batteries. This limited use of this known model is because it induces only minor morphological changes in 2D electrodeposition process; compare the similarity of the 2D dendritic morphologies reported by Wang et al. [50] including the additional surface anisotropy term, and Zhang et al. [24] not using it. However, as we show later, its effect is crucial when modeling 3D dendritic growth.

We modify the phase-field Butler–Volmer equation (reactive Allen–Cahn) [25,42,43] by including the additional surface anisotropy term:

$$\begin{aligned} \frac{\partial\xi}{\partial t} &= -L_\sigma \left\{ \frac{\partial g(\xi)}{\partial\xi} - \nabla \cdot (a^2\nabla\xi) - \sum_{i=1}^3 \frac{\partial}{\partial x_i} \left[ a \frac{\partial a}{\partial \left( \frac{\partial\xi}{\partial x_i} \right)} (\nabla\xi)^2 \right] \right\} \\ &\quad - L_\eta \frac{\partial h(\xi)}{\partial\xi} \left[ e^{\left( \frac{(1-a)F\phi}{RT} \right)} - \tilde{\zeta}_+ e^{\left( \frac{-aF\phi}{RT} \right)} \right]. \end{aligned} \quad (4)$$

### 2.2. Governing equations

Based on phase-field theory, the governing equations for dendrite growth in lithium-metal batteries were discussed in [42,43]. Thus, herein, we only summarize this problem's basic equations, modifying only the phase-field equation for inclusion of the surface anisotropy model (see [42,43] for further details and references). Additionally, we have included a symbols list at the beginning of this paper, with descriptions and associated units for reference.

The lithium-metal batteries dendrite problem using phase field formulation is simulated by the following set of equations: Find  $\Xi =$

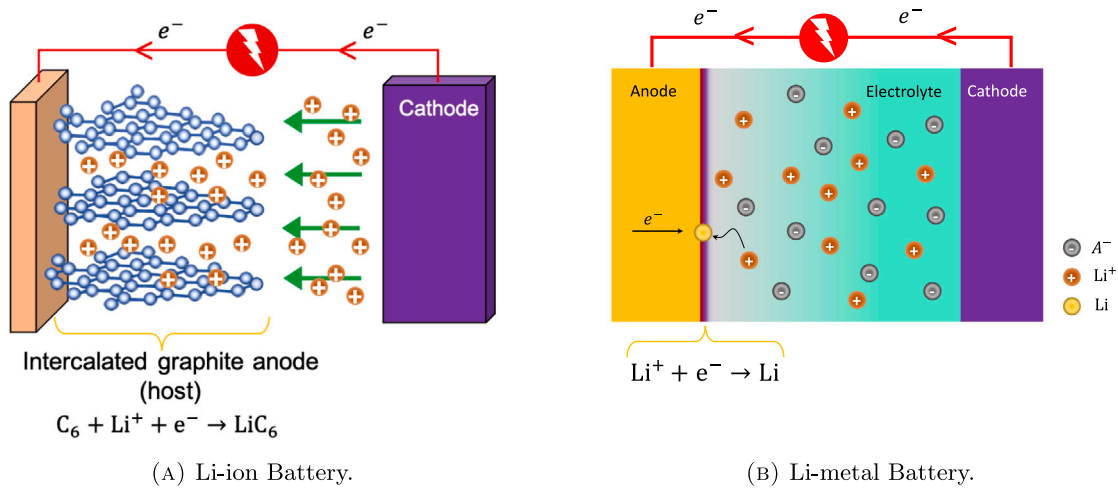


Fig. 1. Schematic comparing charging mechanism and anode's structures between conventional Li-ion (a), and Li-metal (b) batteries. Gray, orange, and yellow spheres represent  $A^-$  anions,  $M^+$  cations, and  $M$  atom, respectively.

$(\xi, \tilde{\zeta}_+, \phi)$  fulfilling

$$\left\{ \begin{array}{l}
 \frac{\partial \xi}{\partial t} = -L_\sigma \left\{ \frac{\partial g(\xi)}{\partial \xi} - \nabla \cdot (a^2 \nabla \xi) \right. \\
 \left. - \sum_{i=1}^3 \frac{\partial}{\partial x_i} \left[ a \frac{\partial a}{\partial (\frac{\partial \xi}{\partial x_i})} (\nabla \xi)^2 \right] \right\} \\
 - L_\eta \frac{\partial h(\xi)}{\partial \xi} \left[ e^{\left( \frac{(1-\alpha)nF\phi}{RT} \right)} \right. \\
 \left. - \tilde{\zeta}_+ e^{\left( \frac{-\alpha nF\phi}{RT} \right)} \right], \quad \text{in } V \times I \\
 \\
 \frac{\partial \tilde{\zeta}_+}{\partial t} = \nabla \cdot \left[ D^{\text{eff}}(\xi) \nabla \tilde{\zeta}_+ + D^{\text{eff}}(\xi) \frac{nF}{RT} \tilde{\zeta}_+ \nabla \phi \right] \\
 - \frac{C_m^s}{C_0} \frac{\partial \xi}{\partial t}, \quad \text{in } V \times I \\
 \\
 nFC_m^s \frac{\partial \xi}{\partial t} = \nabla \cdot [\sigma^{\text{eff}}(\xi) \nabla \phi], \quad \text{in } V \times I \\
 \\
 \xi = \xi_D, \quad \text{on } \partial V_D \times I \\
 \tilde{\zeta}_+ = \tilde{\zeta}_{+D}, \quad \text{on } \partial V_D \times I \\
 \phi = \phi_D, \quad \text{on } \partial V_D \times I \\
 \\
 \nabla \xi \cdot \mathbf{n} = 0, \quad \text{on } \partial V_N \times I \\
 \nabla \tilde{\zeta}_+ \cdot \mathbf{n} = 0, \quad \text{on } \partial V_N \times I \\
 \nabla \phi \cdot \mathbf{n} = 0, \quad \text{on } \partial V_N \times I \\
 \\
 \xi(\mathbf{x}, t_0) = \xi_0, \quad \text{in } V \\
 \tilde{\zeta}_+(\mathbf{x}, t_0) = \tilde{\zeta}_{+0}, \quad \text{in } V \\
 \phi(\mathbf{x}, t_0) = \phi_0, \quad \text{in } V
 \end{array} \right. \quad (5)$$

where  $\xi$  is the phase-field order parameter,  $\tilde{\zeta}_+$  is the lithium-ion concentration, and  $\phi$  is the electric potential;  $V$  is the problem domain with boundary  $\partial V = \partial V_N \cup \partial V_D$ , the subscript  $N$  and  $D$  related to the Neumann and Dirichlet parts (see 2), with outward unit normal  $\mathbf{n}$ , and  $I$  is the time interval.

### 2.3. Implementation details

Following [43], we discretize and solve the set of partial differential equations describing the coupled electrochemical interactions during a battery charge cycle using an open-source finite element library (FEniCS environment) [55]. We use eight-node (tri-linear) hexahedral

elements. We use a message passing interface package MPI4py [56–59] for parallelization and solve nonlinear equations using SNES from PETSc [60]. We perform the simulations using a laptop with a 2.4 GHz processor with 8-core Intel Core i9 and 16 GB 2667 MHz DDR4 RAM (see [43] for further details).

### 3. System layout & properties

Consider a battery cell with a traditional sandwich architecture, with an anode on one side of an electrolyte-filled  $l_x \times l_y \times l_z$  hexagonal domain and a cathode on the other side (represented by a current collector boundary condition — see Fig. 2). This numerical problem has previously been considered in [43] and has been reproduced here for readability. The battery cell undergoes a recharging process under fixed applied electro potential. An artificial nucleation site in the form of an ellipsoidal protrusion (seed) with semi-axes  $r_x, r_y, r_z$ , and center  $(0, l_y, l_z)$  is incorporated at the surface of the anode. The electrolyte within the cell is 1M LiPF<sub>6</sub> EC/DMC 1:1 volume ratio solution [27], whereas the anode is a pure solid material, neglecting any solid phase nanoporosity. The parameters selected for the current study have been presented in Table 1. Further, the following normalization constants are used for length, time, energy and concentration scales:  $h_0 = 1$  [ $\mu\text{m}$ ],  $t_0 = 1$  [s],  $E_0 = 2.5 \times 10^6$  [ $\text{J}/\text{m}^3$ ], and  $C_0 = 1 \times 10^3$  [ $\text{mol}/\text{m}^3$ ] [27].

As the initial condition, a transition zone between solid electrode ( $\xi = 1$ ) and liquid electrolyte ( $\xi = 0$ ) is incorporated, whereby the variables  $(\xi, \tilde{\zeta}_+, \phi)$  vary in the  $x$  spatial direction according to:  $\frac{1}{2} \left[ 1 - \tanh \left( x \sqrt{\frac{W}{2k_0}} \right) \right]$  [65]. For the artificial nucleation case, we modify the initial condition formula, replacing “ $x$ ” by  $h_0 \left[ \left( \frac{x}{r_x} \right)^2 + \left( \frac{y-l_y}{r_y} \right)^2 + \left( \frac{z-l_z}{r_z} \right)^2 - 1 \right]$  within the hyperbolic tangent argument, to account for a smooth transition between the solid seed (lithium metal anode) and the surrounding liquid electrolyte region [43].

#### 3.1. Symmetric boundary conditions

The symmetric nature of spike-like lithium morphology [31,43,47] allows us to reduce the computational cost by using symmetry boundary conditions to model only one-quarter of the domain. Thus, we split the domain in four, and apply Neumann boundary conditions ( $\nabla \xi \cdot \mathbf{n} = 0$ ;  $\nabla \tilde{\zeta}_+ \cdot \mathbf{n} = 0$ ;  $\nabla \phi \cdot \mathbf{n} = 0$ ) to those boundaries facing the center of the domain as depicted in Fig. 3. Therefore, we reduce the size of our computational domain to 25% ( $l_x, l_y/2, l_z/2$ ). We verify our strategy by comparing the previous 3D simulation result using the

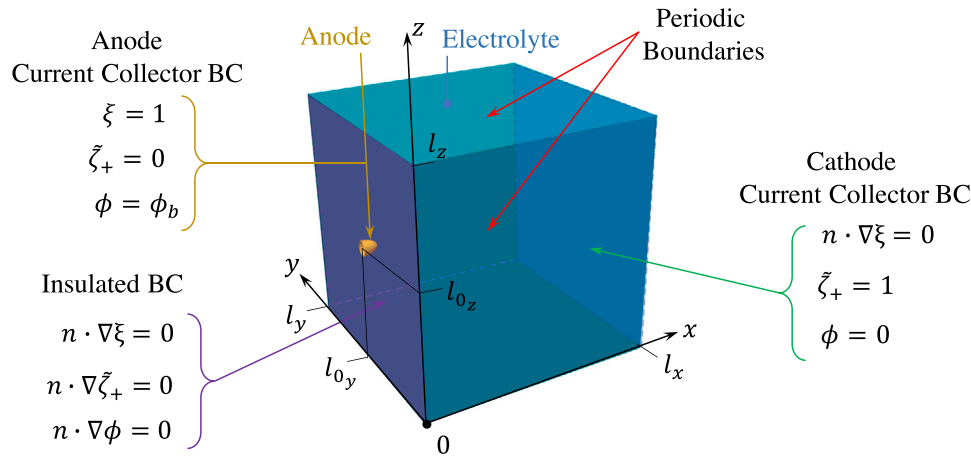


Fig. 2. System layout & boundary conditions for artificial nucleation simulations as defined in [43]. Source: Reproduced with Journal's permission.

Table 1 Simulation parameters [43]. Source: Reproduced with Journal's permission.

Description	Symbol	Real value	Normalized	Source
Exc. current density	$i_0$	30 [A/m <sup>2</sup> ]	30	[61]
Surface tension	$\gamma$	0.556 [J/m <sup>2</sup> ]	0.22	[62,63]
Barrier height	$W$	$W = \frac{12\gamma}{\delta_{PF}} = 4.45 \times 10^6$ [J/m <sup>3</sup> ]	1.78	Computed
Gradient energy coefficient	$\kappa_0$	$\kappa_0 = \frac{3\gamma\delta_{PF}}{2} = 1.25 \times 10^{-6}$ [J/m]	0.5	Computed
Anisotropy strength	$\delta_{aniso}$	0.044	0.044	[52,63]
Anisotropy mode	$\omega$	4	4	[52,53]
Kinetic coefficient	$L_\eta$	$L_\eta = i_0 \frac{\gamma}{nFC_m} = 1.81 \times 10^{-3}$ [1/s]	$1.81 \times 10^{-3}$	Computed
Site density electrode	$C_m^s$	$7.64 \times 10^4$ [mol/m <sup>3</sup> ]	76.4	[27]
Bulk Li-ion concentration	$C_0$	$10^3$ [mol/m <sup>3</sup> ]	1	Computed
Conductivity electrode	$\sigma^s$	$10^7$ [S/m]	$10^7$	[25]
Conductivity electrolyte	$\sigma^l$	1.19 [S/m]	1.19	[64]
Diffusivity electrode	$D^s$	$7.5 \times 10^{-13}$ [m <sup>2</sup> /s]	0.75	[25]
Diffusivity electrolyte	$D^l$	$3.197 \times 10^{-10}$ [m <sup>2</sup> /s]	319.7	[64]

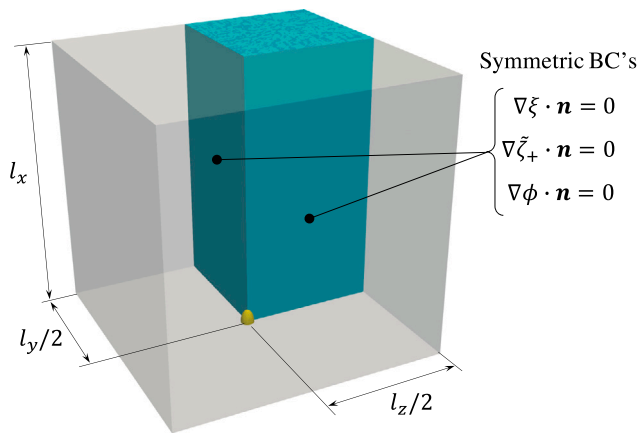


Fig. 3. Symmetric boundary conditions for 3D spike-like simulations.

whole domain (see [43]) and those obtained using symmetric boundary conditions (see Fig. 4(d)). Thus, the symmetric boundary conditions reduce the computational cost, which allows us to use finer meshes in the sensitivity analysis.

Table 2 provides a list of the simulation settings and numerical parameters used in each numerical test presented in this work. For reference, the numerical tests have been enumerated in the order in

which they appear in this paper. Tests 1 to 6 will be used to examine the effect of spatial resolution and phase-field interface thickness, test 7–12 the anisotropy model and mesh rotation, whereas tests 13–14 present the experimental scale model.

#### 4. Phase-field interface thickness to mesh resolution ratio: A sensitivity analysis

The phase-field interface thickness significantly affects the simulated reaction rates [42]. Wider interfaces (larger  $\delta_{PF}$ ) increase the reactive area in the simulation, which induces faster electrodeposition rates. Numerical evidence shows that 1D interface-thickness-independent growth (convergent results) are possible well before reaching the physical nanometer interface width [42,66].

In this section, we perform a sensitivity analysis to study possible mesh-induced effects on the simulated 3D dendrite morphology, propagation rates (dendrite's height vs. time), electrodeposition rates (dendrite's volume vs. time), and energy levels. We compare 3D simulation results for different spatial resolutions and phase-field interface thicknesses. We use the anisotropy model from [43] to enable the comparison with the results reported therein.

A  $80 \times 80 \times 80$  [ $\mu\text{m}^3$ ] computational domain is chosen to conduct this analysis (geometric unit that characterizes a real battery cell [29,67]). Hence, growth rates up to two orders of magnitude faster than those that occur in physical scale cells under the same applied voltage are to be expected, due to the shorter interelectrode separation we use in this case (domain size:  $l_x = 80$  [ $\mu\text{m}$ ]) [43]. Fig. 4 presents a collection of 3D



**Table 2**  
Summary of simulations settings & numerical parameters.

Test	Symmetric BCs	Modified surface anisotropy	Inter-electrode distance	Charging voltage	Interfacial mobility	Mesh size	Mesh rotation	Phase-field interface thickness
#	[-]	[-]	$l_x$ [ $\mu\text{m}$ ]	$\phi_b$ [V]	$L_e$ [ $\text{m}^3/(\text{J s})$ ]	$h$ [ $\mu\text{m}$ ]	[-]	$\delta_{PF}$ [ $\mu\text{m}$ ]
1	✓	✗	80	-0.7	$2.5 \times 10^{-3}$	0.5	✗	2
2	✓	✗	80	-0.7	$2.5 \times 10^{-3}$	0.33	✗	2
3	✓	✗	80	-0.7	$2.5 \times 10^{-3}$	0.25	✗	2
4	✓	✗	80	-0.7	$2.5 \times 10^{-3}$	0.5	✗	1.5
5	✓	✗	80	-0.7	$2.5 \times 10^{-3}$	0.25	✗	1.5
6	✓	✗	80	-0.7	$2.5 \times 10^{-3}$	0.25	✗	1
7	✗	✓	80	-0.7	$2.5 \times 10^{-3}$	0.5	✗	1.5
8	✗	✗	80	-0.7	$2.5 \times 10^{-3}$	0.5	✗	1.5
9	✗	✗	80	-0.7	$2.5 \times 10^{-3}$	0.5	✓	1.5
10	✗	✓	80	-0.7	$2.5 \times 10^{-3}$	0.5	✓	1.5
11	✗	✓	80	-0.7	$2.5 \times 10^{-3}$	0.5	✗	1.5
12	✓	✓	80	-0.7	$2.5 \times 10^{-3}$	0.25	✗	1
13	✗	✓	5000	-0.7	$2.5 \times 10^{-4}$	0.4	✗	1.5
14	✗	✓	5000	-1.4	$2.5 \times 10^2$	0.4	✗	1.5

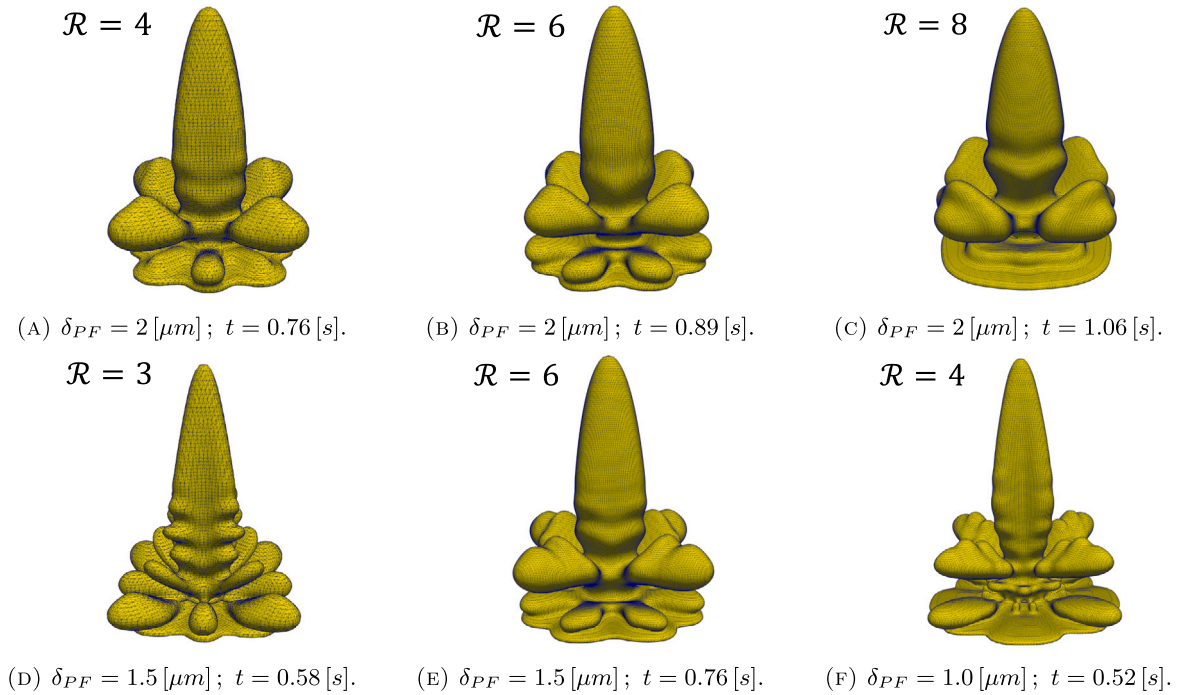


**Fig. 4.** Sensitivity analysis of 3D spike-like lithium dendrite morphology, for different phase-field interface thickness to mesh resolution ratios ( $\mathcal{R} = \delta_{PF}/h$ ), under  $\phi_b = -0.7$  [V] charging potential. Simulated morphologies for  $\delta_{PF} = 2, 1.5$  and  $1$  [ $\mu\text{m}$ ] phase-field interface thickness; mesh grid overlaid with dendrite's morphology. We use dendrite's common height ( $H = 45$  [ $\mu\text{m}$ ]) as the basis of our comparison. Tests 1 to 6.

spike-like lithium dendrite morphologies (isosurface plot of the phase-field variable  $\xi = 0.5$ ), obtained by varying the phase-field interface thickness ( $\delta_{PF} = 1, 1.5$  and  $2$  [ $\mu\text{m}$ ]), and mesh sizes ( $h = 0.5, 0.375$  and  $0.25$  [ $\mu\text{m}$ ]) (Tests 1 to 6). Thus, we test different combinations of phase-field interface thickness to mesh resolution ratios ( $\mathcal{R} = \delta_{PF}/h = 3$  to  $8$ ). We compare dendrite morphologies at the moment they reach a height of  $H = 45$  [ $\mu\text{m}$ ].

Fig. 4 shows spike-like patterns that exhibit morphological similarity, consisting of a main vertical trunk and four side branches (consistent with lithium metal body-centered cubic (bcc) crystallographic arrangement [29]). Smaller phase-field interface thicknesses produce more slender dendritic morphologies (cf. Figs. 4(f) ( $\delta_{PF} = 1$  [ $\mu\text{m}$ ]) and 4(c) ( $\delta_{PF} = 2$  [ $\mu\text{m}$ ])). We use Paraview's mean curvature measurement [68] to analyze the dendrite's tip radius (isosurface plot of the phase-field variable  $\xi = 0.5$ ). Thus, the measured dendrite's tip radius in Fig. 4(f) ( $\delta_{PF} = 1$  [ $\mu\text{m}$ ]) is about  $r_{tip1} = 2.7$  [ $\mu\text{m}$ ], while the computed dendrites' tip radius in Fig. 4(c) ( $\delta_{PF} = 2$  [ $\mu\text{m}$ ]) is

about  $r_{tip2} = 5.3$  [ $\mu\text{m}$ ] (49% larger). The dendrite's maximum cross sectional area, main trunk, in Fig. 4(f) ( $\delta_{PF} = 1$  [ $\mu\text{m}$ ]) is approximately  $A_{max1} = 154$  [ $\mu\text{m}^2$ ], while the computed cross sectional area in Fig. 4(f) ( $\delta_{PF} = 2$  [ $\mu\text{m}$ ]) is about  $A_{max2} = 254$  [ $\mu\text{m}^2$ ] (40% larger). In addition, Fig. 4 shows that increasing the resolution ratio delivers thicker dendritic morphologies ( $\mathcal{R} = \delta_{PF}/h$ ), keeping the phase-field interface thickness constant (more elements at the interface). We compare the morphologies in the first row of Fig. 4 ( $\delta_{PF} = 2$  [ $\mu\text{m}$ ]), against those on the second row of Fig. 4 ( $\delta_{PF} = 1.5$  [ $\mu\text{m}$ ]); in both cases finer mesh resolutions (higher  $\mathcal{R}$ ) lead to less slender and less branched dendritic morphologies.

Fig. 5 depicts the Gibbs free energy evolution  $\Psi = \int_V [f_{ch}(\xi, \zeta_i) + \frac{1}{2} \kappa(\xi)(\nabla \xi)^2 + f_{elec}(\xi, \zeta_i, \phi)] dV$  [43]. The total energy curve is plotted for different simulation set-ups (phase-field interface thickness  $\delta_{PF}$  and mesh resolution ratio  $\mathcal{R}$ ). Fig. 5 shows that in all cases, the systems' discrete free energy does not increase with time (adaptivity delivers discrete energy stable results). We obtain a maximum energy difference

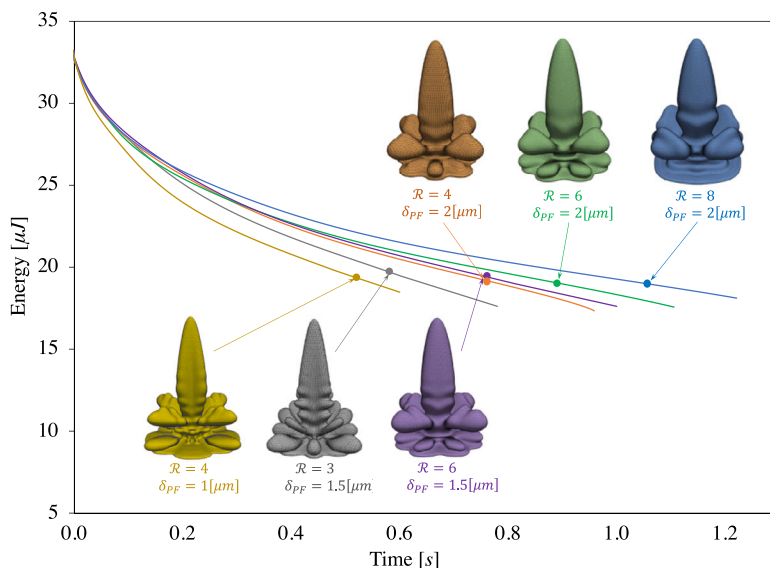


Fig. 5. Comparison of total energy evolution for 3D dendrite growth simulations, for different phase-field interface thickness to mesh resolution ratios ( $\mathcal{R} = \delta_{PF}/h$ ), under  $\phi_b = -0.7$  [V] charging potential. Dendrite morphologies at height  $H = 45$  [ $\mu\text{m}$ ] for reference (colors by phase-field interface thickness and mesh size). Tests 1 to 6.

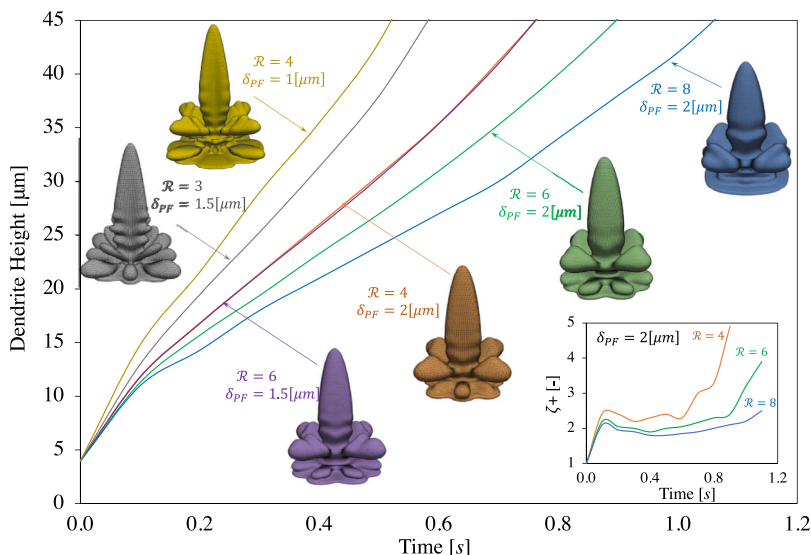


Fig. 6. Comparison of 3D spike-like dendrite propagation rate, for different phase-field interface thickness to mesh resolution ratios ( $\mathcal{R} = \delta_{PF}/h$ ), under  $\phi_b = -0.7$  [V] charging potential. Dendrite morphologies at common height  $H = 45$  [ $\mu\text{m}$ ] for reference (colors by phase-field interface thickness and mesh size). The inset shows maximum Li-ion concentration as a function of time for different  $\mathcal{R} = \delta_{PF}/h$  ratios, using the same phase-field interface thickness ( $\delta_{PF} = 2$  [ $\mu\text{m}$ ]). Tests 1 to 6.

of about 9% ( $t = 0.6$  [s]) between the simulations with the maximum ( $\delta_{PF} = 2$  [ $\mu\text{m}$ ] &  $\mathcal{R} = 8$ ) and minimum ( $\delta_{PF} = 1$  [ $\mu\text{m}$ ] &  $\mathcal{R} = 4$ ) total energy levels (see Fig. 5). In addition, those dendrites sharing a similar level of total energy (represented in green, orange, and purple) exhibit closer morphological resemblance, as the figure shows.

Fig. 6 shows the effect of the phase-field interface thickness and mesh resolution ratio on the dendrite's propagation rate ( $H$  vs.  $t$ ). Smaller phase-field interface thickness produces significantly faster propagation rates. For example, simulation using smaller interface thickness ( $\delta_{PF} = 1$  [ $\mu\text{m}$ ]) exhibits up-to 100% higher growth rates than those obtained under larger interface thickness ( $\delta_{PF} = 2$  [ $\mu\text{m}$ ]). Fig. 6 shows that slower dendrite propagation rates occur as we increase the mesh resolution ratio ( $\mathcal{R} = \delta_{PF}/h$ ), keeping the phase-field interface thickness constant. The inset in Fig. 6 plots the maximum Li-ion concentration surrounding the dendrite's tips ( $\delta_{PF} = 2$  [ $\mu\text{m}$ ]) where the enriched Li-ion concentration decreases as we increase the mesh resolution  $\mathcal{R} = \delta_{PF}/h$  (more accurate solution), leading to slower propagation rates ( $H$  vs.  $t$ ).

Fig. 7 shows the dendrite's volume evolution as a proxy of the overall electrodeposition rate (volume of lithium metal deposited over time). The effect of the phase-field interface thickness and mesh resolution ratio on the overall electrodeposition rate is less significant (percentage-wise) than it is for the dendrite's propagation rate (dendrite's height over time). For example, Fig. 7 shows a maximum electrodeposition rate difference of less than 20% (volume vs. time) between the fastest and slowest simulation results. Thus, faster dendrite's propagation rates occur for smaller phase-field interface thicknesses due to the lithium metal being deposited/spread over a smaller surface area (more slender dendritic morphologies), rather than differences in the overall electrodeposition rate (minor effect).

This analysis shows (see Fig. 7) that for phase field interface thickness 2 [ $\mu\text{m}$ ] or smaller, the simulated electrodeposition rate (volume of lithium metal deposited over time) is relatively insensitive to the numerical parameters ( $\delta_{PF}$  and  $\mathcal{R}$ ). On the other hand, the simulated dendrite propagation rate shows stronger numerical dependencies (see

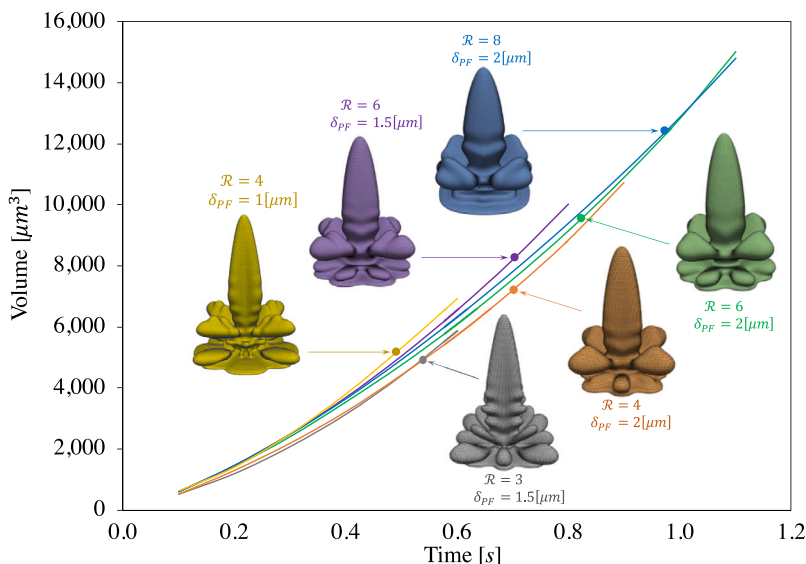


**Fig. 7.** Comparison electrodeposited volume for 3D spike-like dendrite growth simulation, for different phase-field interface thickness to mesh resolution ratios ( $\mathcal{R} = \delta_{PF}/h$ ), under  $\phi_b = -0.7$  [V] charging potential. Tests 1 to 6.

Fig. 6), affecting the level of realism of our results. Thus, propagation predictions presented here should only be taken as a comparison indicator between numerical tests, as we work towards smaller phase-field interface thickness to increase the accuracy of our simulations.

### 5. 3D simulations using modified surface anisotropy

We evaluate the performance of the surface anisotropy representation model for metal anode battery simulations (see Section 2.1). We perform numerical tests to gain insight into the benefits of this modification compared with the results previously obtained in Section 4 and the preceding 3D simulation work [43]. These studies consist of 3D phase-field simulations of lithium electrodeposition during battery charge state to explore three-dimensional highly branched “spike-like” dendritic patterns [31,46,47].

#### 5.1. Comparison of simulated patterns: Surface anisotropy model

We study the performance of the modified surface anisotropy representation (4) using a 3D numerical experiment (Test 7) and comparing the resulting morphologies with those obtained for single nucleus simulations using the standard anisotropy representation (see Fig. 4(d)). We use the simulation setup as defined in Section 3. Fig. 8 depicts the evolution of the simulated dendrite morphology together with the enriched lithium-ion concentration ( $\tilde{c}_+ > 1$ ), with peak values of  $\tilde{c}_+ = 2.3$ . Consistent with previous simulations, the obtained dendritic morphology consists of the main trunk and sets of four equal orthogonal branches developing to the sides. The side branches grow up to 18  $\mu\text{m}$  long (60% longer than in previous simulations), and 5 to 10  $\mu\text{m}$  width. Furthermore, the side branches growth is not perpendicular to the main trunk but at an angle of about 25° to 50°, with a separation of about 4 to 8  $\mu\text{m}$  between branches. These results show improved morphological similarity with dendritic patterns observed in lithium experiments performed by Tatsuma et al. [47].

Fig. 9(a) plots the evolution of the surface energy for the 3D lithium patterns we simulate, revealing equivalent energy levels (less than 4% difference) when compared against the results previously obtained using the initial, non-modified, anisotropy representation. Thus, the numerical experiment demonstrates that the modified anisotropy representation did not significantly affect the surface energy. Additionally, Fig. 9(b) characterizes the dendrites’ structure by tracking

the volume-specific area ( $\mu\text{m}^2/\mu\text{m}^3$ ). We compute the volume-specific area average ratios of 0.83 and 0.78  $[\mu\text{m}^2/\mu\text{m}^3]$  for the single nucleus and modified anisotropy simulations, respectively. The slightly lower surface area/volume ratio of the modified anisotropy representation (−6%) indicates the dendrite growth has fewer but larger branches.

#### 5.2. Mesh orientation effect for different surface anisotropy representations

We further compare the behavior of the standard (Test 9) and modified anisotropy representation behavior (Test 10) by studying the mesh orientation’s effect on each simulated pattern. So far, the simulations results use structured meshes aligned with the Cartesian axes. Unlike previous 3D simulations, we now proceed to redistribute the mesh (node’s mapping) by performing a 25° rotation around the  $x$ -axis, as depicted in Fig. 10. Thus, here we test the dendrite’s sensitivity to the mesh orientation. Fig. 11 compares the dendrite morphologies using the standard anisotropy representation, using Cartesian (Test 8), as well as 25° rotated mesh distribution (Test 9) (see Fig. 10). We compare dendrite’s cross sections (horizontal slices) at positions  $L_O = 5, 10, 15$  & 25  $\mu\text{m}$ . The analysis reveals an alignment of dendrites’ side branches to the mesh orientation (angular offset), with no major differences in terms of the simulated dendrite’s shapes.

Fig. 12 shows simulated dendrite morphologies under the rotated mesh distribution, using the standard (Test 9) and modified (Test 10) surface anisotropy representations. Now, we analyze the dendrite’s side branches orientation  $\theta$  at fixed positions  $L_O = 5, 15, 25$  & 30  $\mu\text{m}$  (horizontal slices of dendrite’s contour plot). We define the orientation  $\theta$  as the inclination of the line that crosses the geometry by passing through its center and connecting the two farthest points of the contour (see Fig. 12). We compare dendrite morphologies at the moment they reach a height of  $H = 45$   $\mu\text{m}$ . The analysis of the dendrite’s side branches (horizontal slices) in Fig. 12 reveals that the standard anisotropy representation is more sensitive to the orientation of the mesh. For example, orientation analysis in Fig. 12(a) depicts dendrite’s rotation angles of around  $\theta = 23^\circ$ , evidently aligned with the 25° of rotation imposed to the mesh. The side branches, due to the modified surface anisotropy representation (4) exhibit significantly smaller rotations of about  $\theta = 4^\circ$ , using the same simulation conditions (see Fig. 12(b)). Thus, the modified anisotropy model shows reduced sensitivity with respect to the mesh.



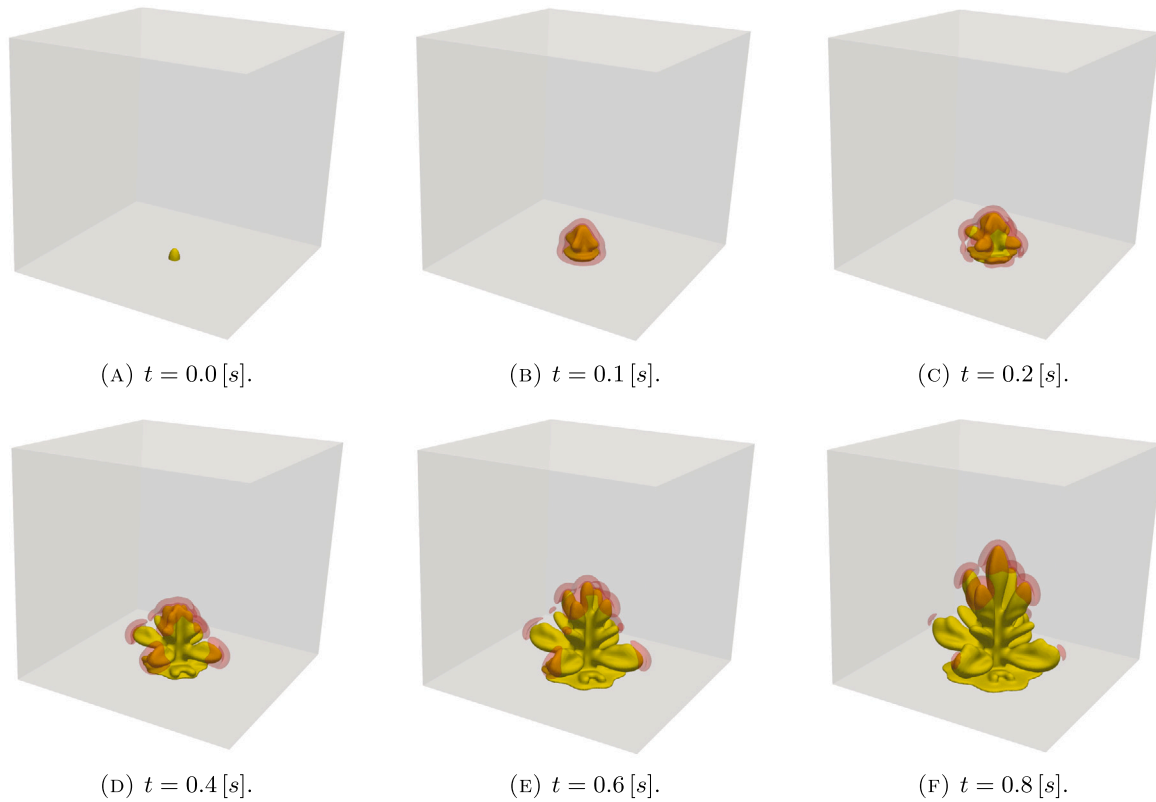


**Fig. 8.** Simulated lithium dendrite morphology with modified surface anisotropy representation, under  $\phi_b = -0.7$  [V] applied voltage. Yellow isosurface plot of the phase-field variable  $\xi$  represents the electrodeposited lithium metal. Orange volumes represent the enriched Li-ion concentration ( $\tilde{c}_+ > 1$ ) in the electrolyte region. Cube domain set as  $80 \times 80 \times 80$  [ $\mu\text{m}^3$ ]. Phase-field interface thickness  $\delta_{PF} = 1.5$  [ $\mu\text{m}$ ] & mesh size  $h = 0.5$  [ $\mu\text{m}$ ]. Test 7.

### 5.3. 3D orientation of lithium crystal: A surface anisotropy-based strategy

Given the random nature of the nucleation process, we need to deal with some degree of randomness and uncertainty when determining the preferred growth direction of the dendrite's crystal in the battery. The orientation of the crystal, determined by the orientation of the surface anisotropy, will direct the preferred direction of growth of the lithium dendrite. Thus, we adapt this well-known crystal growth model for solidification in [54] to electrodeposition dendrite growth. We define a material system of coordinates  $(\tilde{x}, \tilde{y}, \tilde{z})$ , in which each axis corresponds to the  $\langle 100 \rangle$  direction of a cubic lattice. The following coordinate transformation  $\mathbb{T}$  is used between the coordinate systems of  $(x, y, z)$  and  $(\tilde{x}, \tilde{y}, \tilde{z})$ :

$$\begin{Bmatrix} \frac{\partial \xi}{\partial \tilde{x}} \\ \frac{\partial \xi}{\partial \tilde{y}} \\ \frac{\partial \xi}{\partial \tilde{z}} \end{Bmatrix} = \underbrace{\begin{bmatrix} 1 & 0 & 0 \\ 0 & \cos \theta_x & \sin \theta_x \\ 0 & -\sin \theta_x & \cos \theta_x \end{bmatrix} \begin{bmatrix} \cos \theta_y & 0 & \sin \theta_y \\ 0 & 1 & 0 \\ -\sin \theta_y & 0 & \cos \theta_y \end{bmatrix} \begin{bmatrix} \cos \theta_z & \sin \theta_z & 0 \\ -\sin \theta_z & \cos \theta_z & 0 \\ 0 & 0 & 1 \end{bmatrix}}_{\mathbb{T}} \begin{Bmatrix} \frac{\partial \xi}{\partial x} \\ \frac{\partial \xi}{\partial y} \\ \frac{\partial \xi}{\partial z} \end{Bmatrix} \quad (6)$$

where  $\theta_x$ ,  $\theta_y$ , and  $\theta_z$  are the rotation angles around the x, y, and z axes, respectively.

We use (6) to compute the gradient of the phase-field variable ( $\nabla \xi$ ) and use it in the surface anisotropy expression (1). Therefore, we can assign random values to each of the rotation angles ( $\theta_x, \theta_y, \theta_z$ ) to control the preferred growth direction of the lithium dendrite and side branches. We test the proposed strategy (Test 10) by applying a  $\theta_x = 35^\circ$  rotation ( $\theta_y = \theta_z = 0^\circ$ ) to the lithium surface anisotropy when using a Cartesian mesh. Fig. 13 shows the simulated spike-like lithium dendrite morphology after  $t = 0.7$  [s]. The top-view analysis 13(a)

reveals that this rotation resulted in a dendrite rotation of about  $\theta = 31^\circ$  under the applied anisotropy angle, showing the effectiveness of the proposed strategy.

### 5.4. Mesh size effect for different surface anisotropy representations

Following Section 4, we study the spatial sensitivity of the modified surface representation under mesh refinement (Test 12). Given spike-like lithium dendrite symmetry (see Fig. 8), we use symmetry condition of Section 3.1 to reduce the computation cost and improve the mesh resolution. Thus, we model only one-quarter of the domain, using a  $200 \times 100 \times 100$  tensor-product mesh with a mesh spacing of  $0.25$  [ $\mu\text{m}$ ] in the region of interest (bottom half of the domain).

The simulation forms a spike-like and highly branched morphology (see Fig. 14). We calculate the electric field distribution by differentiating the resolved electric potential  $\vec{E} = -\nabla \phi$ . Fig. 14 shows how the electric field localizes in the vicinity of the dendrite tip [43]. Consistent with previous simulations [43], the electric field distribution leads to an enriched Li-ion concentration due to the strong migration from the surrounding regions [22].

Fig. 15 compares the effect of the mesh resolution and phase-field interface thickness on the simulated morphologies, with and without the presence of the modified surface anisotropy term. For the modified surface anisotropy representation, smaller phase-field interface thickness ( $\delta_{PF}$ ) and finer mesh resolution ( $h$ ) lead to more branched and detailed dendritic patterns. However, in the standard case, finer mesh leads to less branched microstructures (see Fig. 15(c)).

Despite the morphological differences mentioned above, the computed lithium electrodeposition average rate in this case ( $10,800$  [ $\mu\text{m}^3/\text{s}$ ]) is within analogous simulation results under coarser mesh resolution ( $9150$  [ $\mu\text{m}^3/\text{s}$ ], see Fig. 9(b)), as well as simulation result using the standard anisotropy representation, using coarse and fine

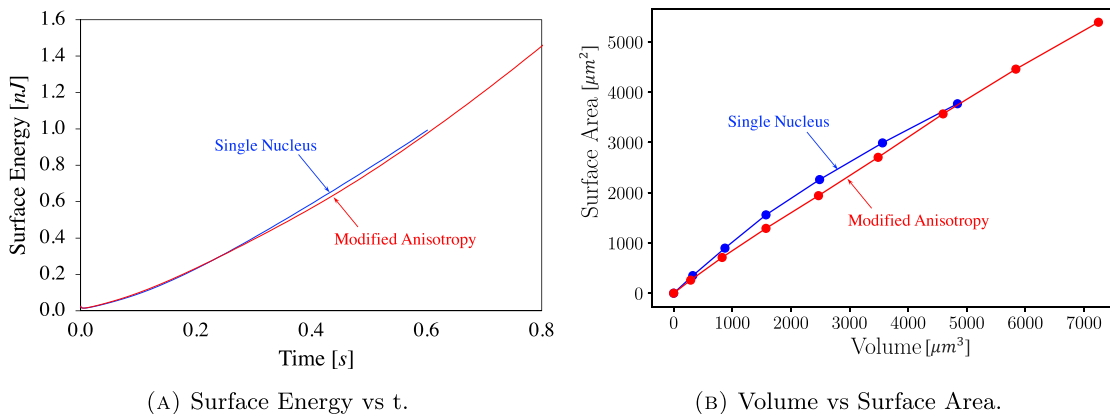


Fig. 9. Comparison between 3D simulations of lithium dendrite growth (single nucleus initial vs. modified surface anisotropy), in terms of the evolution of the surface energy **a**, and volume vs surface area ratio over time **b**. Tests 4 & 7.

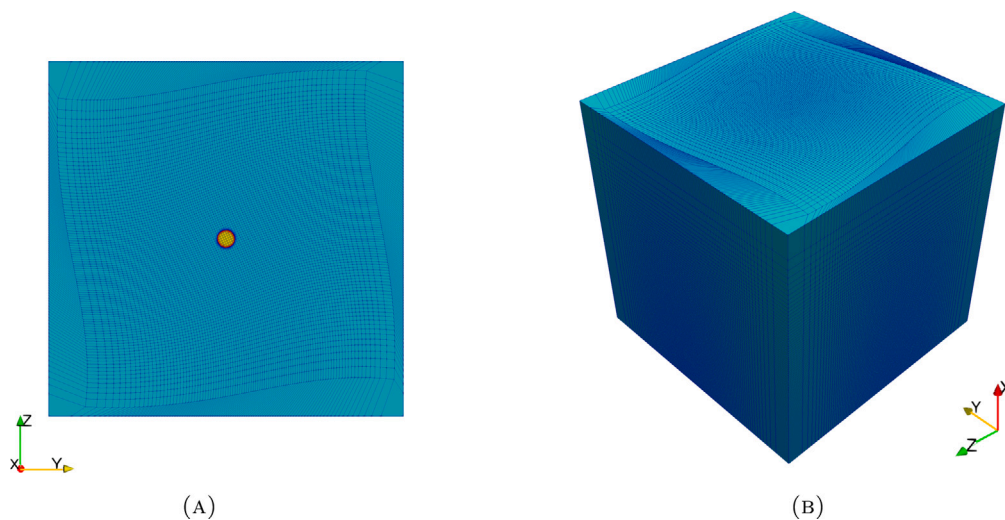


Fig. 10. Bottom **a** & perspective **b** views of the 3D mesh with 25° rotation around the x-axis (node's mapping). Cube domain set as  $80 \times 80 \times 80 \mu m^3$ .

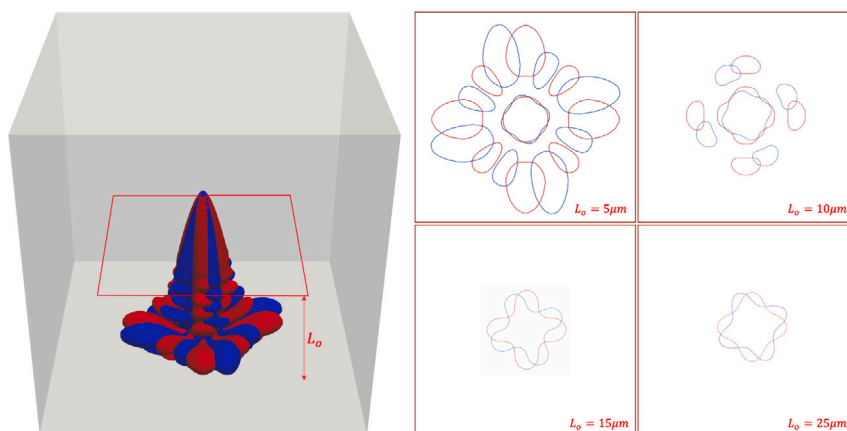
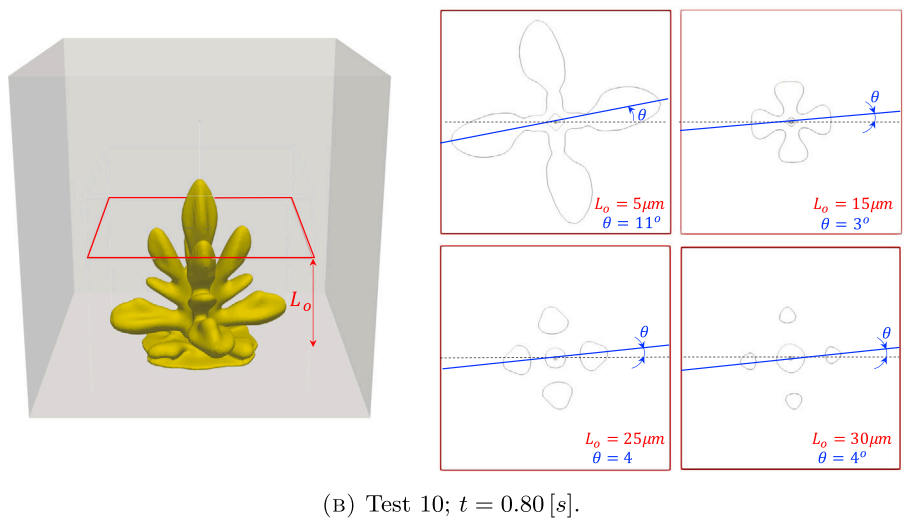
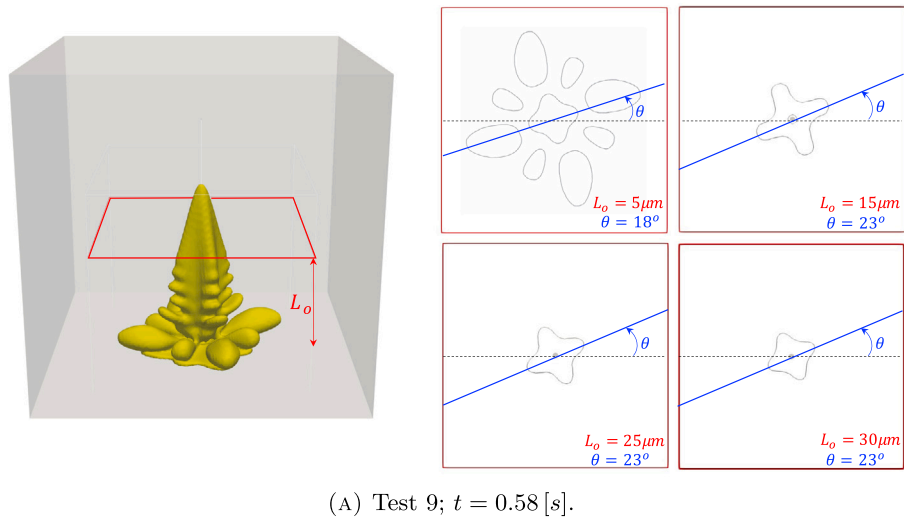
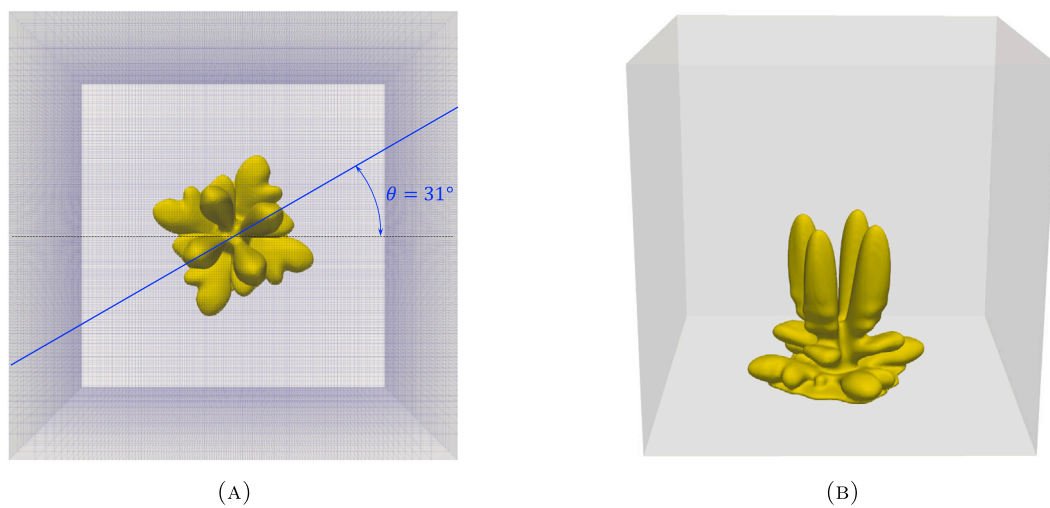


Fig. 11. Overlay of 3D simulated dendrite morphologies (non-modified anisotropy representation), obtained under Cartesian mesh (red — Test 8), and 25° rotated mesh around the x-axis (blue — Test 9). Horizontal slices of the dendrite's contour plots at positions  $L_0 = 5, 10, 15$  &  $25 \mu m$  depict the angular offset between the morphologies.



**Fig. 12.** 3D simulation results using a single artificial protrusion with the initial **a** (Test 9) and the modified surface anisotropy representation **b** (Test 10), under a 25° rotated mesh around the  $x$ -axis (longitudinal). Horizontal slices of the dendrite's contour plot at positions  $L_o = 5, 15, 25$  &  $30$  [ $\mu\text{m}$ ] depict the orientation  $\theta$  of the side branches. We use dendrite's common height ( $H = 45$  [ $\mu\text{m}$ ]) as the basis of our comparison.



**Fig. 13.** Top **a** & perspective **b** views of the 3D spike-like lithium dendrite simulation, with  $\theta_s = 35^\circ$  rotation of the surface anisotropy. Top view overlaid with mesh shows that dendrite's orientation is not aligned with the Cartesian axes. Test 11.

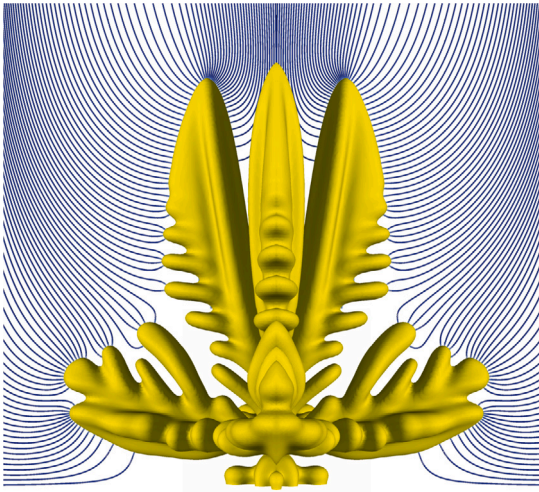


Fig. 14. Overlay of simulated dendritic pattern with electric field distribution (blue streamlines) under the modified surface anisotropy representation at time  $t = 0.7$  [s]. We combine in this Fig. 4 symmetric copies. Streamline plane set at  $y = 40$  [ $\mu\text{m}$ ]. Test 12.

mesh options (10,100 to 12,400 [ $\mu\text{m}^3/\text{s}$ ], see Fig. 7). These results show that using the modified surface anisotropy representation is robust in relation to the rate of electrodeposition (volume of lithium metal deposited over time), showing relatively low sensitivity to numerical parameters of our choice ( $\delta_{PF}$  and  $\mathcal{R}$ ). In practice, the amount of dendritic lithium directly reduces the Coulombic efficiency of the battery [69]. Therefore, we envisage a future application of our model in evaluating Coulombic efficiency reduction due dendrite's formation in rechargeable lithium batteries.

## 6. Experimental-scale 3D simulations of lithium dendrite formation

This section evaluates the performance of the modified surface anisotropy model (see Section 2.1) in experimental-scale interelectrode distances. We map the nodal distribution concentrating the nodes in the region of interest, inspired by experimental and simulation results. The increased domain size affects the lithium electrodeposition behavior by increasing the interelectrode distance. We discuss the lithium dendrite propagation rates and morphologies for different charging voltages.

### 6.1. Meshing strategy for experimental-scale 3D simulations

The high computational cost of detailed 3D simulations of lithium dendrite formation at scale of the whole-cell is a well-known challenge of electrodeposition simulations [26,29,43]. A limiting factor is the domain size, which imposes practical restrictions on the 3D simulations. Previously, we chose a domain size of ( $80 \times 80 \times 80$  [ $\mu\text{m}^3$ ]) that ensures the simulation volume at an affordable computational cost. But this short domain (electrode separation of  $l_x = 80$  [ $\mu\text{m}$ ]) induces dendrite growth rates that are two orders of magnitude higher than those observed experimentally [43].

A detailed analysis of lithium dendrite experiments reveals that, despite the interelectrode separation distance in experimental cells, which ranges from 1 to 10 [mm] [70–72], the lithium dendrites effectively occupy up to 20% of the interelectrode space. Thus, we focus on this area of interest, the region/volume of the experimental cell where lithium dendrites develop, near the anode surface. Furthermore, previous simulation results show that the spatial distribution of the variables in the bulk region (outside the area of interest) exhibit either constant values, such as  $\xi = 0$  and  $\tilde{\zeta}_+ = 1$ , or small electric potential gradients  $\nabla\phi$ . This weak variation indicates that only a few elements

may adequately capture the bulk behavior. At the same time, we assign most computational resources to the area presenting the steepest gradients of  $\xi$ ,  $\tilde{\zeta}_+$  and  $\phi$ , representing a small portion of the whole domain.

This section applies the modified anisotropy representation in 3D simulations targeting experimental time and length scales. We describe a simple meshing strategy that exploits the aforementioned distribution by combining uniform node's mapping in the portion of the physical domain where the lithium electrodeposition process occurs (finer and regular mesh), with an exponential increment of the mesh size as we move away from the electrode into the electrolyte's bulk region. Thus, we use a 3D structured mesh with eight-node hexahedral elements. Within the bulk region, in particular in the  $x$ -direction  $x_r = 2^j \times x_u$  with  $j = 1, 2, \dots, n$ ; where  $x_u$  is the node's  $x$  coordinate normalized by  $l_x$ , before mapping (uniform distribution), and  $x_r$  is the node's mapped coordinate. The exponential function transitions smoothly by doubling the element size when moving away from the area of interest into the bulk region. This focussed-mesh distribution in the area of interest and subsequent stretching allow us to achieve experimental interelectrode distances with only a few additional elements. Consequently, although the detailed portion of our domain ( $l_{x_u}$ ) remains the same ( $80 \times 80 \times 80$  [ $\mu\text{m}^3$ ]), we are now able to avoid simulations with higher-than-normal dendrite's growth rates, by achieving experimental interelectrode distances ( $l_x$  up-to 5000 [ $\mu\text{m}$ ]).

Thus, we select a geometrical unit that characterizes a real cell structure [29,67]. We choose a computational domain of  $5000 \times 80 \times 80$  [ $\mu\text{m}^3$ ]. Fig. 2 summarizes the boundary conditions we apply. Lateral dimensions remain unchanged in this case ( $l_y = l_z = 80$  [ $\mu\text{m}^3$ ]), which along with periodic boundary conditions applied on the lateral faces, generates a  $80$  [ $\mu\text{m}$ ]  $\times$   $80$  [ $\mu\text{m}$ ] nucleation arrangement surrounding the simulated morphology (neighboring dendrites). The implemented approach constitutes a more realistic alternative than modeling a single isolated dendrite [70,71]. Furthermore, neighboring dendrites act as a barrier (charge repulsion effect) that limits the side development of the simulated electrodeposit beyond the domain's boundaries.

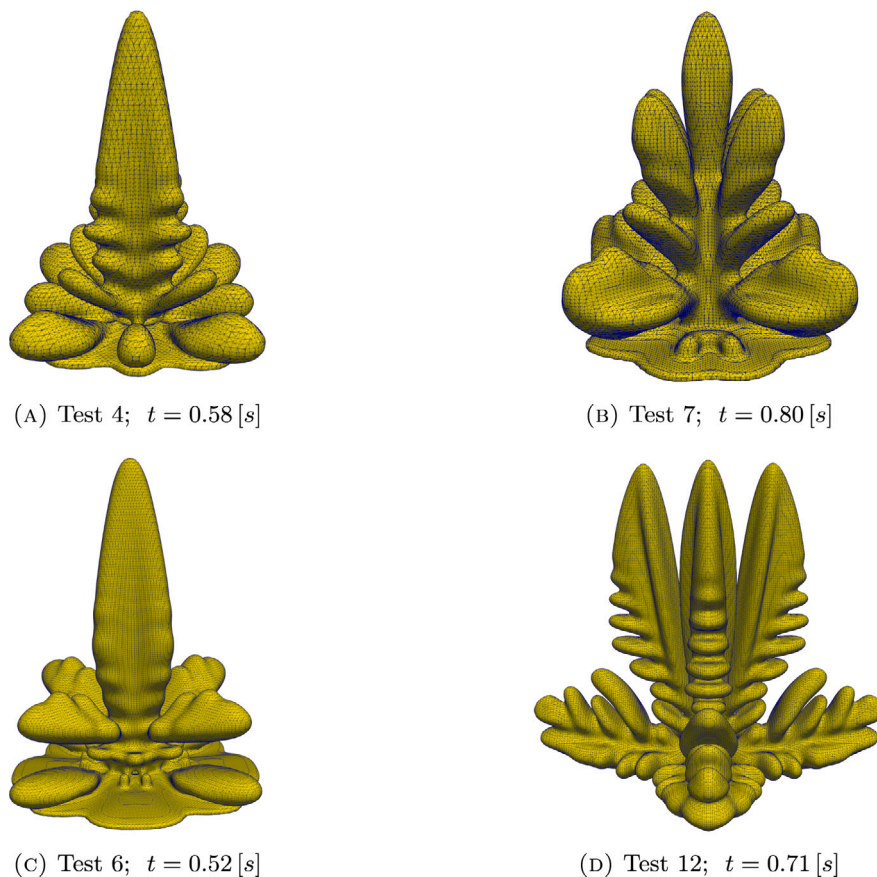
We use a  $180 \times 100 \times 100$  tensor-product mesh, partitioned into eight processors identified with different colors in Fig. 16. Fig. 16 shows that the tensor-product mesh can efficiently allocate resources in the region of interest ( $l_{x_u}$ ).

### 6.2. Experimental-scale 3D simulations.

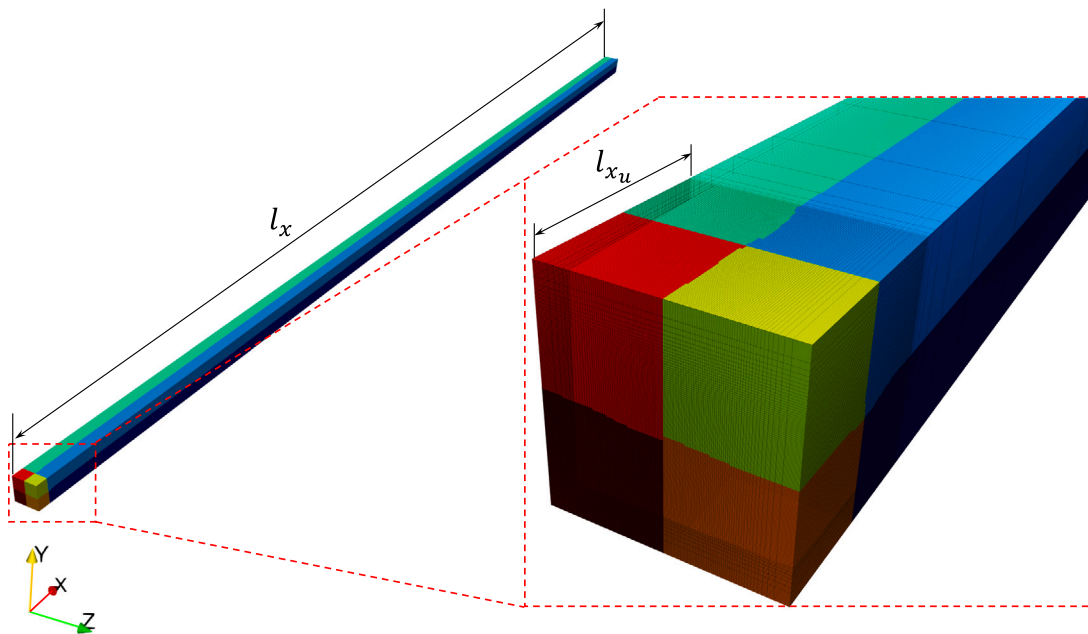
This section presents 3D phase-field simulations of lithium dendrite formation to study dendritic patterns formed under  $\phi_b = -0.7$  [V] (Test 13) and  $\phi_b = -1.4$  [V] charging potential (Test 14), using experimental-scale interelectrode distance ( $l_x = 5000$  [ $\mu\text{m}$ ]). We use artificial nucleation regions, ellipsoidal protrusions (seeds) with semi-axes  $4$  [ $\mu\text{m}$ ]  $\times$   $2$  [ $\mu\text{m}$ ]  $\times$   $2$  [ $\mu\text{m}$ ], and centers located at  $(y, x, z) = (0, 38, 38)$ ,  $(0, 42, 38)$ ,  $(0, 38, 42)$  and  $(0, 42, 42)$  [43]. We modify the initial condition, by introducing a constant electric potential gradient in the liquid electrolyte region, from  $\phi = \phi_b$  at the electrode–electrolyte interface, to  $\phi = 0$  at  $x = l_x$  (cathode), which corresponds to the experimental observations by Nishida et al. [71]. They measured the initiation periods (time transient) for dendrite precursors to start to grow (become visible under an optical microscope) between 4 to 140 s [71]; shorter initiation times occur under larger applied current density. Therefore, sufficiently developed dendrite nuclei may take several seconds to appear, depending on the electrodeposition conditions. This time is sufficient for developing the electric potential gradient in the electrolyte. In addition, the initial conditions for  $\xi$  and  $\tilde{\zeta}_+$  remain the same [43].

Fig. 17 depicts the dendritic electrodeposition of lithium under  $\phi_b = -0.7$  [V] charging potential (Test 13). This setup yields realistic simulation time scales due to the larger interelectrode distance we employ [70]. Stationary propagation rates (dendrite's tip speed) of around  $0.2$  [ $\mu\text{m}/\text{s}$ ] are reached after 70 s of simulation (see Fig. 20(a)). The simulated growth rates are larger than those reported by Nishikawa





**Fig. 15.** Comparison of fully developed lithium dendrite morphologies under  $\phi_b = -0.7$  [V] charging potential. Yellow isosurface plot of the phase-field variable  $\xi$ , overlaid with the mesh grid, represents the lithium dendrite morphology. Top row (a & b) presents simulation results obtained under coarser mesh resolution ( $h = 0.5$  [ $\mu\text{m}$ ] &  $\delta_{PF} = 1.5$  [ $\mu\text{m}$ ]). Bottom row (c & d) depicts results obtained under finer resolution ( $h = 0.25$  [ $\mu\text{m}$ ] &  $\delta_{PF} = 1$  [ $\mu\text{m}$ ]). Left column (a & c) correspond to simulated morphologies using the non-modified surface anisotropy representation, and the right column (b & d) allocates dendritic patterns under the modified anisotropy representation. We use dendrite's common height ( $H = 45$  [ $\mu\text{m}$ ]) as the basis of our comparison. Cube domain set as  $80 \times 80 \times 80$  [ $\mu\text{m}^3$ ] in all cases.



**Fig. 16.** 3D mesh partition in 8 processors, each one represented by a different color. Magnified view of the region of interest ( $l_{xu} \ll l_x$ ), showing a uniform to exponential mapping transition while moving into the bulk region of the domain.

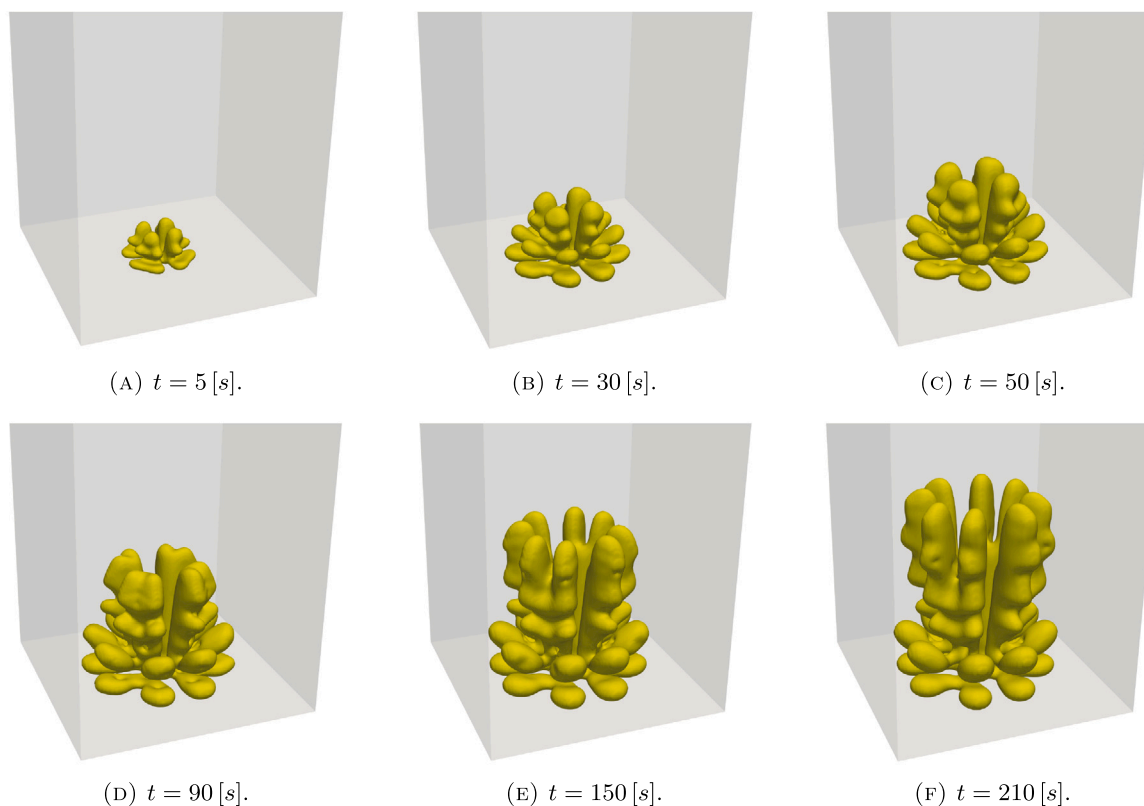


Fig. 17. 3D lithium dendrite simulation with modified anisotropy representation, under  $\phi_b = -0.7$  [V] charging potential. Hexagonal domain set as  $5000 \times 80 \times 80$  [ $\mu\text{m}^3$ ]. Test 13.

et al. [70] in experimental measurements of lithium dendrite growth in 1M LiPF<sub>6</sub> electrolyte ( $0.06$  [ $\mu\text{m}/\text{s}$ ]) due in part to the higher (almost double) applied current density in our model. Our results are within the range of lithium dendrite growth rates reported by Nishida et al. [71] ( $0.25 - 0.55$  [ $\mu\text{m s}^{-1}$ ]) using a different electrolyte type (LiTFSI). Unlike previous 3D simulations, forming spike-like patterns [43], this case yields less branched, blunt tip, finger-like morphologies. The observed morphological difference is a consequence of the spatial distribution of the electrostatic potential in the electrolyte ( $\phi$ ). Although the applied electric potential remains the same ( $\phi_b = -0.7$  [V]) the larger interelectrode distance results in a significantly different electric field distribution ( $\vec{E} = -\nabla\phi$ ). The electric field surrounding the electrodeposit region can be 60 times smaller than in previous simulations lowering the current density (consistent with the change ratio in the interelectrode distance  $5000$  [ $\mu\text{m}$ ] /  $80$  [ $\mu\text{m}$ ] =  $62.5$ ). This weaker current density results in a weaker action of the electric migration over the distribution of lithium ions in the electrolyte. Thus, lithium ions are less prone to accumulate around dendrite tips due to the counteracting influence of diffusion due to the concentration gradient, producing less branched and blunt morphologies.

The lower electric field effect is in agreement with experimental observations by Chae et al. [48], where a variation of the separation between the electrodes revealed a considerable difference in the electrochemical deposition of lithium (experiments under  $1$  [ $\text{mA}/\text{cm}^{-2}$ ] applied current density). Chae et al. [48] observed that the lithium deposition behavior and morphology changed from “hazardous” needle- and moss-like dendritic structures to “safer” morphologies (smooth and round shaped surface) as interelectrode spacing increases. The variation of lithium deposition behavior was ascribed to a difference in the Li-ion concentration distribution. Thus, when under shorter interelectrode separation ( $<500$  [ $\mu\text{m}$ ]), lithium electrodeposition occurs closer to the high Li-ion concentration regions (formed by the release of Li-ions from the counter electrode), producing a non-uniform directional deposition of lithium. Sharp dendritic structures can grow and penetrate porous

separators, which are potentially dangerous as they can create a short battery circuit [73]. On the other hand, larger electrode separations ( $2000$  and  $4000$  [ $\mu\text{m}$ ]) lead to a more uniform deposition, without any angular edges or sharp tips, due to lower Li-ion concentration and electric potential gradients [48]. Although the current density applied in the present simulation is lower than in previous numerical examples, it remains well above the limiting current density of the system, about  $i_{lim} = 2$  [ $\text{mA}/\text{cm}^{-2}$ ] [74] (SEI-free lithium growth [73]).

Fig. 18 shows that the fully developed lithium dendrite morphology ( $t = 210$  [s]) resides within the region of interest (well-resolved portion of the domain:  $\leq 80$  [ $\mu\text{m}$ ]), which makes-up only 1.6% of the whole domain. Although the system size is similar to previous 3D simulations presented in this work ( $5,400,000$  degrees of freedom), the temporal evolution is slower, increasing the computational time by four times.

Next, we present a 3D phase-field simulation of lithium dendrite formation under more negative applied voltage  $\phi_b = -1.4$  [V] (Test 14). We use the setup of the previous experiment, with the sole difference of the applied voltage  $\phi_b$ . We adjust the interfacial mobility parameter  $L_\sigma$  to the newly applied electro potential to achieve the right balance between the phase-field interface energy term and the electrochemical reaction contribution (see Table 2) [42]. Fig. 19 depicts the evolution of the lithium dendrite ( $\xi$  isosurface). As in the previous experimental-scale case, we obtain realistic simulated time scale, with stationary dendrite propagation rates of about  $0.4$  [ $\mu\text{m}/\text{s}$ ] (see Fig. 20(b)). The higher propagation rate in this case is due to the higher applied current density (from  $\phi_b = -0.7$  to  $-1.4$  [V] charging potential), which agrees with experimental results, where higher current densities produce faster electrodeposition and dendrite propagation rates [61,70,75]. Furthermore, we see that computed dendrite propagation rates are within the range of lithium dendrite experiments reported by Nishida et al. [71].

The simulation produces a spike-like, symmetric, and highly branched pattern, with morphological resemblance to previous dendritic deposits obtained under shorter interelectrode distance [43]. Fig. 21

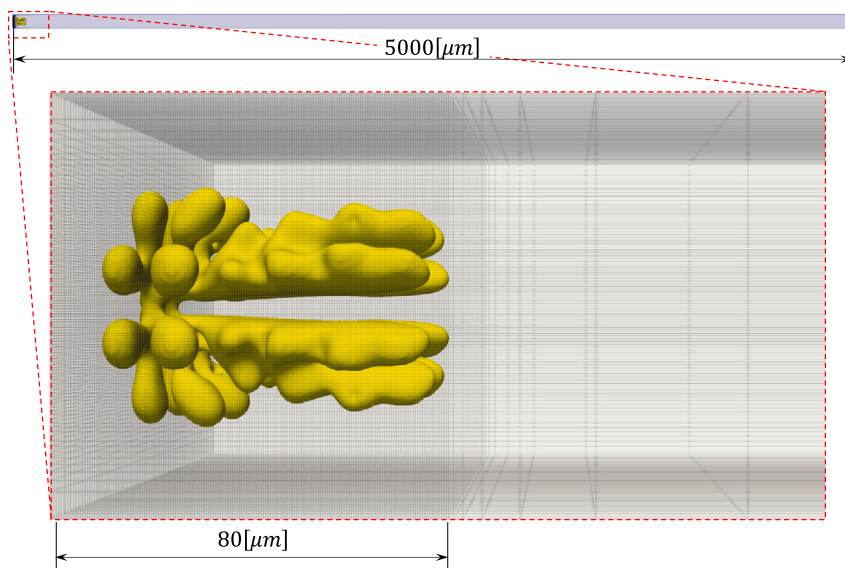


Fig. 18. 3D mesh overlaid with simulated lithium dendrite morphology at  $t = 210$  [s] ( $\phi_b = -0.7$  [V]). Magnified view of the region of interest ( $l_{x_0} \ll l_x$ ), showing a uniform to exponential mapping transition while moving into the bulk region. Test 13.

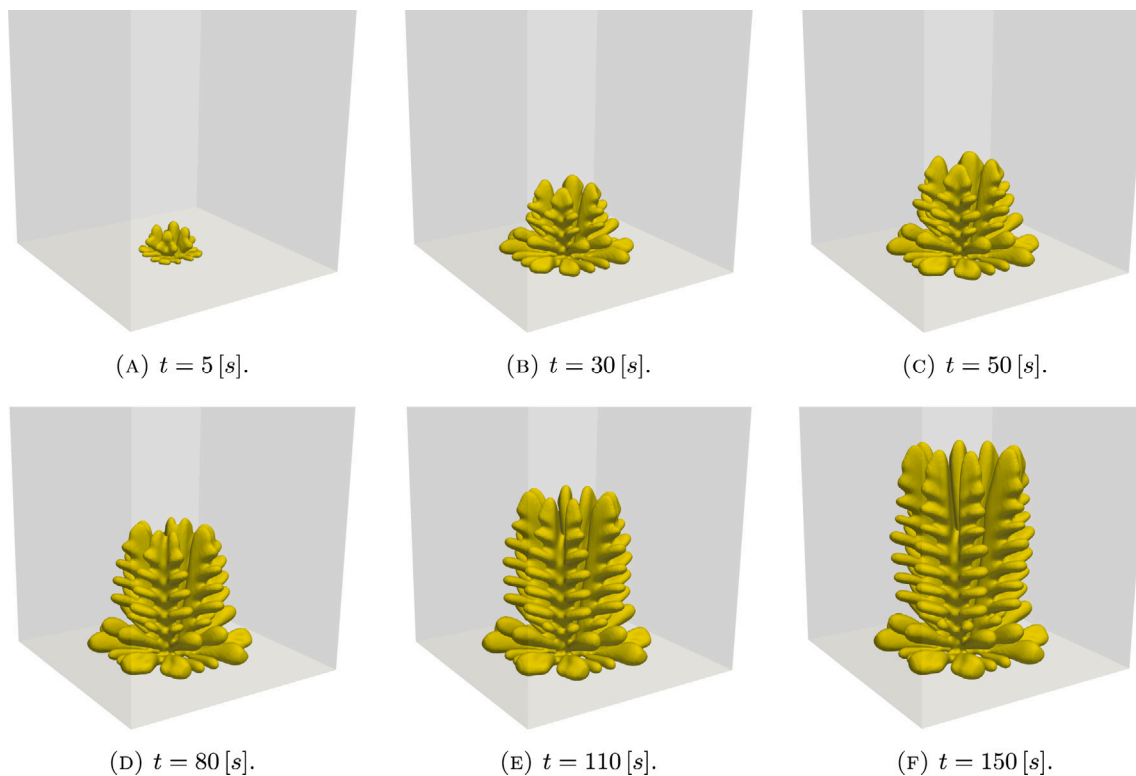


Fig. 19. 3D lithium dendrite simulation with modified anisotropy representation, under  $\phi_b = -1.4$  [V] charging potential. Hexagonal domain set as  $5000 \times 80 \times 80$  [ $\mu\text{m}^3$ ]. Test 14.

shows the evolution of the simulated spike-like dendritic morphology and the Li-ion concentration profile ( $\tilde{c}_+$ ) extending over  $400$  [ $\mu\text{m}$ ] in the stack direction ( $x$ ); where the deposition process depletes the lithium-ion concentration close to the electrode (shown in blue). This behavior contrasts with smaller-scale simulations presented earlier in this work and in previous work [43], where Li-ion concentration enriches the dendrite tips due to large electric migration (see Fig. 9). This dendrite-tip enrichment can happen in a close-to-short-circuit condition (short interelectrode distance). Nevertheless, our simulations indicate that lower electro-potential gradients, such as those obtained under experimental-scale interelectrode distances, do not generate high Li-ion

concentration around the dendrite tips (competition between electric migration and Li-ion diffusion due to the concentration gradient). This observation is in agreement with experimental measurements of Li-ion surface concentration by Nishida et al. [71], where the concentration of Li-ion near the electrode surface was reduced from  $1$  M (initially) to less than  $0.1$  M, after a few tens of seconds of electrodeposition, depending on the experiment's conditions.

We obtain apparent morphological differences from the previous dendritic lithium electrodeposition simulation under the experimental-scale domain (compare with Fig. 17). Although in this case, the electric field ( $\vec{E} = -\nabla\phi$ ) surrounding the electrodeposit region remains low

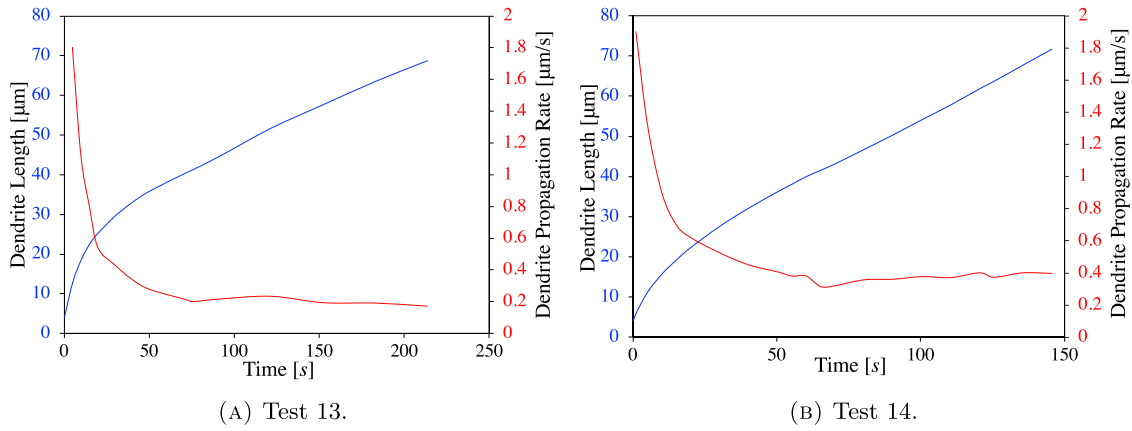


Fig. 20. Simulated 3D lithium dendrite propagation plot. Dendrite length (blue) & propagation rate (red) vs. time for applied voltages: (a)  $\phi_b = -0.7$  [V] (Test 13), and (b)  $\phi_b = -1.4$  [V] (Test 14).

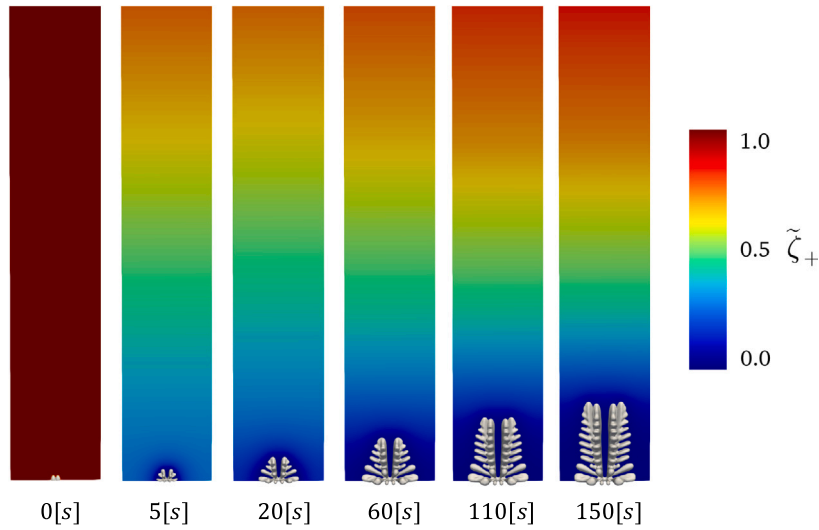


Fig. 21. Evolution of the spatial distribution of lithium-ion concentration, overlaid with dendrite morphology. Contour plane set at  $y = 35$  [ $\mu\text{m}$ ], display of first 400 [ $\mu\text{m}$ ] portion of the domain. Experimental interelectrode distance  $l_x = 5000$  [ $\mu\text{m}$ ], and applied voltage  $\phi_b = -1.4$  [V]. Test 14.

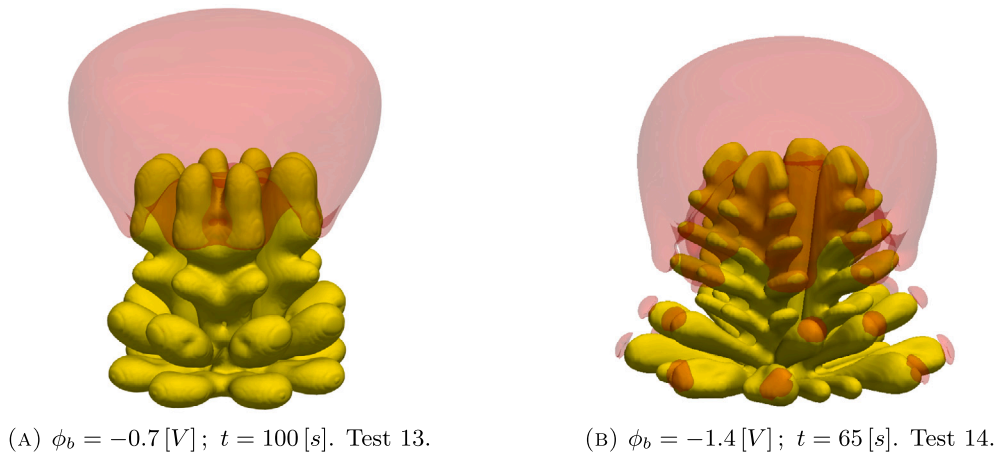


Fig. 22. Comparison of lithium-ion concentration gradients for (a)  $\phi_b = -0.7$  [V] (Test 13), and (b)  $\phi_b = -1.4$  [V] (Test 14), applied voltage. Electrolyte regions with higher lithium-ion concentration gradient ( $\|\nabla \tilde{\zeta}_+\| > 0.005$ ) represented with red volumes. Interelectrode distance  $l_x = 5000$  [ $\mu\text{m}$ ]. We use dendrite's common height ( $H = 45$  [ $\mu\text{m}$ ]) as the basis of our comparison.

relative to previous simulations with shorter interelectrode separation  $\sim 30$  times smaller; the larger charging voltage ( $\phi_b = -1.4$  [V]) induces a spike-like and highly branched dendrite (over-limiting current density condition). This result agrees with previous two-dimensional

phase-field studies investigating the effect of the applied voltage on the electrodeposit's morphological structure. Increasing the applied voltage produces faster dendrite formation with the tip splitting phenomenon [25], changing from a needle or finger-like structure to



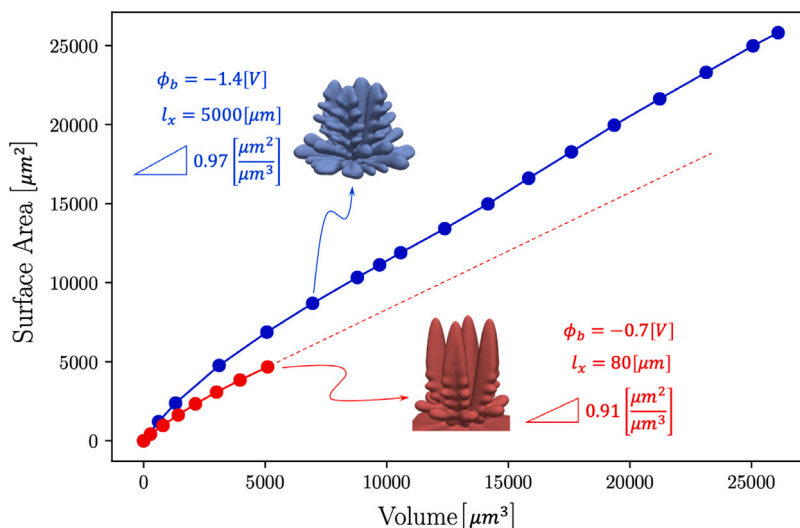


Fig. 23. Morphological comparison between 3D simulations of spike-like multi-nuclei dendrite growth, smaller-scale with non-modified anisotropy representation (red) [43] (reproduced with Journal's permission), and experimental-scale with modified anisotropy representation (blue — Test 14), in terms of the evolution of volume vs. surface area ratio.

a tip splitting or spike-like pattern [30]. The reactive term of the phase-field equation, see (4), is exponentially affected by the electric potential through  $\eta_a = \phi - E^\theta$ . The applied voltage increases the degree of polarization on the electrode, affecting the deposition and accumulation of lithium on the anode surface, which leads to changes in the morphology of lithium dendrites [30]. One verifies this by inspecting the Li-ion concentration gradient  $\|\nabla\tilde{c}_+\|$  in the electrolyte region surrounding the dendrites morphologies. Fig. 22 shows a comparison between the experimental-scale simulation results obtained under different charging voltages:  $\phi_b = -0.7$  [V] (Fig. 22(a)), and  $\phi_b = -1.4$  [V] (Fig. 22(b)). Electrolyte regions with higher lithium-ion concentration gradients ( $\|\nabla\tilde{c}_+\| > 0.005$ ) are represented with red volumes. Thus, higher lithium-ion concentration gradients appear in the vicinity of the dendrites' tips and side branches in Fig. 22(b) leading to a spike-like, highly branched dendritic lithium (resembling the previously observed electric-migration versus Li-ion diffusion gradient competition happening here at a smaller scale). In contrast, Fig. 22(a), under lower applied voltage, only presents higher lithium-ion concentration gradients in the vicinity of upper tips of the dendrite triggering vertical and less branched growth. Therefore, the spike-like lithium morphologies forming under over-limiting current density (fast battery charge) [31] can occur either using a large electric field ( $\vec{E} = -\nabla\phi$ ) surrounding the electrodeposition region (close-to-short-circuit condition) or under a large applied voltage  $\phi_b$  (fast battery charge). This forcing produces strong electric migration, inducing a movement of Li-ion from less concentrated neighboring regions and gather around dendrite tips, leading to highly branched dendritic lithium.

Following [72], we characterize the morphology by tracking the dendrites' volume-specific area ( $\mu\text{m}^2/\mu\text{m}^3$ ). Fig. 23 compares the growth of the deposited volume versus the surface area for the 3D spike-like lithium pattern we simulate (short interelectrode separation vs. experimental-scale results).

Despite differences in the time and length scales between these simulations, we obtain similar volume-specific area average ratios; 0.91 and 0.97  $[\mu\text{m}^2/\mu\text{m}^3]$ , for smaller-scale and experimental-scale simulations, respectively. The higher surface area/volume ratio indicates a more branched shape in the experimental-scale simulation. Both cases are within the volume-specific results reported for experimental formation of dendrites in zinc batteries (0.86 and 1.04  $[\mu\text{m}^2/\mu\text{m}^3]$ ) [72] (the literature lacks experimental data for quantitative characterization of the spike-like lithium morphologies).

**Remark 1.** The similar area/volume average ratios between the dendritic microstructures formed using the experimental-scale simulation domain and the deposition patterns obtained under the short interelectrode distance setup (close-to-short-circuit condition) opens the possibility of using small-scale (lower-cost) 3D simulations. For example, the earlier ones in this work may be a useful testing tool to assess and adjust different 3D strategies before moving into more expensive, well-resolved larger-scale 3D simulations.

Fig. 24 tracks the number of side branches formed over time. The simulation produces stationary ratios of about 0.5 branch per second [1/s]. The number of branches is determined via visual inspection of the simulated dendrite morphology. We compare our simulation results with the experimental measurement of zinc dendrites, due to the lack of experimental data in the literature for the characterization of spike-like lithium morphologies. Yufit et al. [72] reported values between 0.19 and 0.92 branches per second [1/s] for experimental formation of “spruce tree”-like dendrites in zinc batteries under  $\phi_b = -1.6$  [V] applied voltage, and 3000  $[\mu\text{m}]$  interelectrode separation. Thus, we observe that the simulated branching dynamic is in agreement with experimental data.

Fig. 25 depicts the behavior of the time-adaptive integrator during the 150 [s] of simulation. Initial convergence is achieved by starting with a small time-step of  $\Delta t_0 = 10^{-8}$  [s], followed by an increase in size, until reaching a stationary value of about  $\Delta t_{n+1} = 0.05$  [s] (almost two orders of magnitude larger than previous simulations under smaller interelectrode distance [43]). The weighted truncation error  $e_{n+1}$  (blue) remains near the minimum tolerance limit ( $10^{-9}$ ) during the whole simulation. The estimated error does not grow exponentially as in previous cases [43] since the lithium dendrite remains far away from the positive electrode (propagation rate does not accelerate).

Standard discrete approximations do not inherit the a priori nonlinear stability relationship satisfied by phase-field models, expressed as a time-decreasing free-energy functional (see, e.g., [76–78] for discussions on energy stable time-marching methods). Therefore, we study the energetic evolution of our system, using our adaptive time integration scheme for the experimental-scale phase-field simulation. We observe that the systems' total discrete free energy  $\Psi = \int_V (f_{\text{ch}} + f_{\text{grad}} + f_{\text{elec}}) dV$  does not increase with time (see Fig. 26). Therefore, we achieve discrete energy stable results in experimental-scale simulations using our second-order backward-difference (BDF2) time-adaptive marching scheme [43], although the method is not provably stable energetically. Moreover, while the system's surface and chemical energies

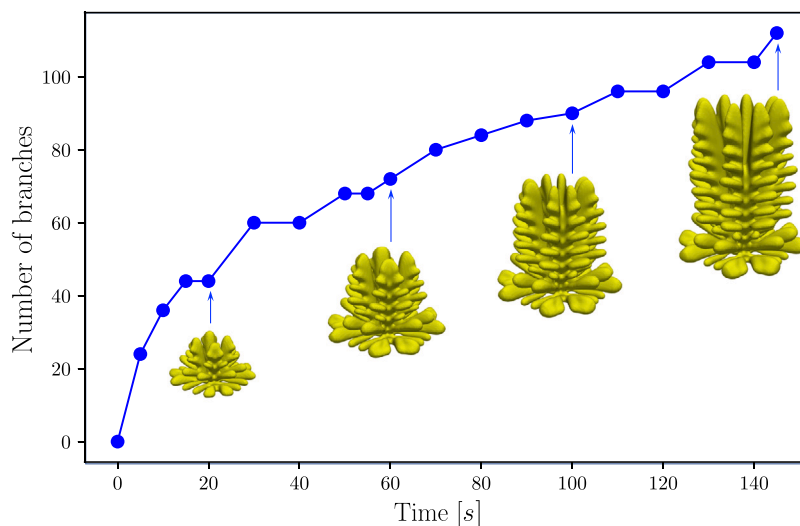


Fig. 24. Morphological analysis of 3D spike-like dendrite growth simulation in terms of number of side branches developed over time. Experimental interelectrode distance  $l_s = 5000$  [ $\mu\text{m}$ ], and applied voltage  $\phi_b = -1.4$  [V]. Test 14.

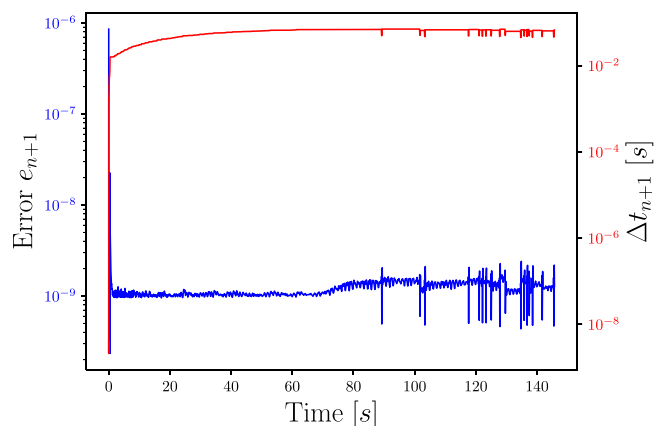


Fig. 25. Time adaptivity plot for 3D lithium dendrite growth simulation under  $\phi_b = -1.4$  [V] charging potential, and experimental-scale interelectrode distance (5000 [ $\mu\text{m}$ ]). Test 14.

grow as the area of the lithium deposit increase, the electrostatic energy decreases in time. This behavior, previously observed in smaller scale 3D simulations, is consistent with the battery charging process, storing the applied electrostatic energy as electrochemical energy. The inset in Fig. 26 shows that the surface energy of the fully developed pattern is almost four times larger than the surface energy computed in [43] for the smaller-scale simulation. The proportionately four-times larger surface area in the experimental-scale case (see Fig. 23) explains this scaling.

## 7. Conclusions

We use phase-field modeling to investigate the electrodeposition process that forms dendrites within lithium-metal batteries (LMB). We analyze the dendrite formation in domains with various sizes using both, short (80 [ $\mu\text{m}$ ]) and experimental-scale (5000 [ $\mu\text{m}$ ]) interelectrode separation. Through a resolution sensitivity analysis, we assess the mesh-induced effect on the simulated 3D dendrite morphology, propagation rates (dendrite's height vs. time), electrodeposition rates (dendrite's volume vs. time), and energy levels. Well-resolved simulations showed that the modified model (3D representation of the surface

anisotropy) preserves the robustness in the rate of lithium electrodeposition, while showing less sensitivity to the mesh orientation.

We test our model under different charging conditions ( $\phi_b = -0.7$  [V] and  $\phi_b = -1.4$  [V]) on a (larger) experimental-scale domain (higher computational cost). Unlike simulations using shorter interelectrode separation, we observe no enrichment of Li-ion concentration surrounding the dendrite morphology at experimental scale ( $\tilde{\zeta}_+ < 1$ ). However, electric migration continues to cause lithium cations to move from less concentrated surrounding regions and accumulate around dendrite tips (identified as higher lithium-ion concentration gradients  $\|\nabla\tilde{\zeta}_+\| > 0.005$ ), triggering spike-growing and highly branched dendritic lithium in the case of  $\phi_b = -1.4$  [V] charging potential. In contrast, under 50% lower applied voltage ( $\phi_b = -0.7$  [V]), high lithium-ion concentration gradients are only present in the vicinity of the upper tips of the dendrite, triggering vertical and less branched growth, with smoother and rounder surface shapes [48].

Thus, our analysis at the experimental scale confirms what was previously observed under smaller-scale simulations: dendrite formation is connected to the competition between the lithium cation diffusion and electric migration, generating an uneven distribution of  $\text{Li}^+$  on the electrode surface [43]. This fact gives insight into inhibition strategies focusing on enhancing the diffusion of lithium ions to achieve a more uniform concentration field on the anode surface, leading to lower dendrite formation propensity [79–92].

Given our understanding of the process, in future work we may add other physical aspects to the simulation; our 3D phase-field model coupled with additional fields will allow us to gain insight into other aspects of dendrite formation and assess some of the proposed strategies for dendrite suppression. Thus, strategies from 2D phase-field models available in the literature could be followed; for example, the current model does not consider heat transfer to simulate the thermal effect during the lithium dendrite growth process. Thermal-induced ion-diffusion may allow us to study dendrite suppression under high operating temperatures [28,41]. Also, the contribution from transport (forced advection) will allow us to study the effect of electrolyte hydrodynamics on the dendrite morphology in flow batteries [32,93], and electrochemical-mechanical phase-field models to study the role of stress in lithium dendrites [29,31]. We will also develop provably unconditionally stable second-order time accurate methods that may deliver larger time-step sizes for phase-field models [76–78,94,95], adaptive mesh refinement strategies [96], and improvement of the parallel computation efficiency [37,96].

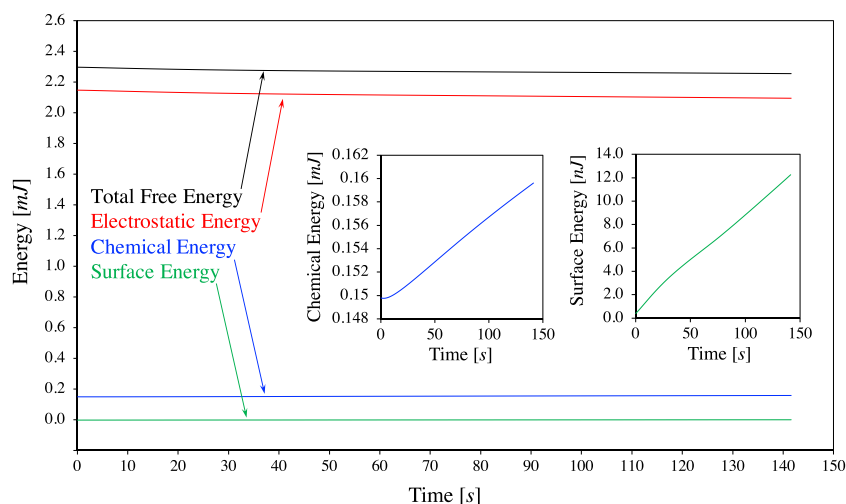


Fig. 26. Energy time series for 3D spike-like dendrite growth simulation with modified anisotropy representation, under  $\phi_b = -1.4$  [V] applied voltage, and interelectrode distance  $l_x = 5000$  [ $\mu\text{m}$ ]. The insets plot the increasing chemical and surface energy in smaller scale for better appreciation. Test 14.

### CRedit authorship contribution statement

**Marcos E. Arguello:** Methodology, Investigation, Writing – original draft. **Nicolás A. Labanda:** Methodology, Investigation, Writing – original draft. **Victor M. Calo:** Methodology, Resources, Writing – review & editing. **Monica Gumulya:** Conceptualization, Writing – review. **Ranjeet Utikar:** Conceptualization, Supervision. **Jos Derksen:** Conceptualization, Writing – review & editing.

### Declaration of competing interest

The authors declare that they have no known competing financial interests or personal relationships that could have appeared to influence the work reported in this paper.

### Data availability

Data will be made available on request.

### Acknowledgments

This work was supported by the sponsorship of a Curtin International Postgraduate Research Scholarship (CIPRS), Australia and the Aberdeen-Curtin Alliance PhD Scholarship, Australia. This publication was also made possible in part by the Professorial Chair in Computational Geoscience at Curtin University. This project has received funding from the European Union's Horizon 2020 research and innovation programme under the Marie Skłodowska-Curie, Australia grant agreement No 777778 (MATHROCKS). The Curtin Corrosion Centre and the Curtin Institute for Computation kindly provide ongoing support.

### References

- [1] IEA, Global energy review 2021, 2021, Paris.[Online] <https://www.iea.org/reports/global-energy-review-2021> [Accessed: 2021-06-07].
- [2] Vaclav Smil, Energy Transitions: Global and National Perspectives, ABC-CLIO, 2016.
- [3] IEA, Global energy review: CO2 emissions in 2021, 2022, Paris.[Online] <https://www.iea.org/reports/global-energy-review-co2-emissions-in-2021-2> [Accessed: 2021-06-07].
- [4] Mahesh Kumar, Social, economic, and environmental impacts of renewable energy resources, in: Kenneth Eloghene Okedu, Ahmed Tahour, Abdel Ghani Aissaou (Eds.), Wind Solar Hybrid Renewable Energy System, IntechOpen, Rijeka, 2020, chapter 11.
- [5] Max Roser Hannah Ritchie, Pablo Rosado, Energy, Our World Data (2020) <https://ourworldindata.org/energy>.
- [6] V Fernão Pires, Enrique Romero-Cadaval, D Vinnikov, I Roasto, JF Martins, Power converter interfaces for electrochemical energy storage systems—A review, *Energy Convers. Manage.* 86 (2014) 453–475.
- [7] Yanguang Li, Jun Lu, Metal–air batteries: Will they be the future electrochemical energy storage device of choice? *ACS Energy Lett.* 2 (6) (2017) 1370–1377.
- [8] Martin Winter, Brian Barnett, Kang Xu, Before li ion batteries, *Chem. Rev.* 118 (23) (2018) 11433–11456.
- [9] Ying Zhang, Tong-Tong Zuo, Jelena Popovic, Kyungmi Lim, Ya-Xia Yin, Joachim Maier, Yu-Guo Guo, Towards better li metal anodes: challenges and strategies, *Mater. Today* 33 (2020) 56–74.
- [10] L. Mathieu, C. Mattea, From dirty oil to clean batteries, in: *Battiers Vs Oil: A Systematic Comparison of Material Requirements*, European Federation for Transport and Environment AISBL, Brussels, 2021.
- [11] Dingchang Lin, Yayuan Liu, Yi Cui, Reviving the lithium metal anode for high-energy batteries, *Nature Nanotechnol.* 12 (3) (2017) 194–206.
- [12] Qingyu Wang, Bin Liu, Yuanhao Shen, Jingkun Wu, Zequan Zhao, Cheng Zhong, Wenbin Hu, Confronting the challenges in lithium anodes for lithium metal batteries, *Adv. Sci.* 8 (17) (2021) 2101111.
- [13] Louise Frenck, Gurmukh K Sethi, Jacqueline A Maslyn, Nitash P Balsara, Factors that control the formation of dendrites and other morphologies on lithium metal anodes, *Front. Energy Res.* 7 (2019) 115.
- [14] Aniruddha Jana, R. Edwin Garcia, Lithium dendrite growth mechanisms in liquid electrolytes, *Nano Energy* 41 (2017) 552–565.
- [15] Alejandro A Franco, Alexis Rucci, Daniel Brandell, Christine Frayret, Miran Gaberscek, Piotr Jankowski, Patrik Johansson, Boosting rechargeable batteries R&D by multiscale modeling: myth or reality? *Chem. Rev.* 119 (7) (2019) 4569–4627.
- [16] J.E. Guyer, W.J. Boettinger, J.A. Warren, G.B. McFadden, Phase field modeling of electrochemistry. I. Equilibrium, *Phys. Rev. E* 69 (2004) 021603.
- [17] J.E. Guyer, W.J. Boettinger, J.A. Warren, G.B. McFadden, Phase field modeling of electrochemistry. II. Kinetics, *Phys. Rev. E* 69 (2004) 021604.
- [18] Yasushi Shibuta, Yoshinao Okajima, Toshio Suzuki, Phase-field modeling for electrodeposition process, *Sci. Technol. Adv. Mater.* 8 (6) (2007) 511–518, Nanoionics - Present and future prospects.
- [19] Yoshinao Okajima, Yasushi Shibuta, Toshio Suzuki, A phase-field model for electrode reactions with Butler–Volmer kinetics, *Comput. Mater. Sci.* 50 (1) (2010) 118–124.
- [20] Linyun Liang, Yue Qi, Fei Xue, Saswata Bhattacharya, Stephen J. Harris, Long-Qing Chen, Nonlinear phase-field model for electrode-electrolyte interface evolution, *Phys. Rev. E* 86 (2012) 051609.
- [21] Martin Z. Bazant, Theory of chemical kinetics and charge transfer based on nonequilibrium thermodynamics, *Acc. Chem. Res.* 46 (5) (2013) 1144–1160.
- [22] Linyun Liang, Long-Qing Chen, Nonlinear phase field model for electrodeposition in electrochemical systems, *Appl. Phys. Lett.* 105 (26) (2014) 263903.
- [23] David R. Ely, Aniruddha Jana, R. Edwin Garcia, Phase field kinetics of lithium electrodeposition, *J. Power Sources* 272 (2014) 581–594.
- [24] H.-W. Zhang, Z. Liu, L. Liang, L. Chen, Y. Qi, S.J. Harris, P. Lu, L.-Q. Chen, Understanding and predicting the lithium dendrite formation in li-ion batteries: Phase field model, *ECS Transactions* 61 (8) (2014) 1–9.
- [25] Lei Chen, Hao Wei Zhang, Lin Yun Liang, Zhe Liu, Yue Qi, Peng Lu, James Chen, Long-Qing Chen, Modulation of dendritic patterns during electrodeposition: A nonlinear phase-field model, *J. Power Sources* 300 (2015) 376–385.
- [26] Daniel A. Cogswell, Quantitative phase-field modeling of dendritic electrodeposition, *Phys. Rev. E* 92 (2015) 011301.

- [27] Zijian Hong, Venkatasubramanian Viswanathan, Phase-field simulations of lithium dendrite growth with open-source software, *ACS Energy Lett.* 3 (7) (2018) 1737–1743.
- [28] H.H. Yan, Y.H. Bie, X.Y. Cui, G.P. Xiong, L. Chen, A computational investigation of thermal effect on lithium dendrite growth, *Energy Convers. Manage.* 161 (2018) 193–204.
- [29] Vitaliy Yurkiv, Tara Foroozan, Ajaykrishna Ramasubramanian, Reza Shahbazian-Yassar, Farzad Mashayek, Phase-field modeling of solid electrolyte interface (SEI) influence on Li dendritic behavior, *Electrochim. Acta* 265 (2018) 609–619.
- [30] Wenyu Mu, Xunliang Liu, Zhi Wen, Lin Liu, Numerical simulation of the factors affecting the growth of lithium dendrites, *J. Energy Storage* 26 (2019) 100921.
- [31] Aniruddha Jana, Sang Inn Woo, KSN Vikrant, R Edwin Garcia, Electrochemomechanics of lithium dendrite growth, *Energy Environ. Sci.* 12 (12) (2019) 3595–3607.
- [32] Keliang Wang, Yu Xiao, Pucheng Pei, Xiaotian Liu, Yichun Wang, A phase-field model of dendrite growth of electrodeposited zinc, *J. Electrochem. Soc.* 166 (10) (2019) D389.
- [33] Rui Zhang, Xin Shen, Xin-Bing Cheng, Qiang Zhang, The dendrite growth in 3D structured lithium metal anodes: Electron or ion transfer limitation? *Energy Storage Mater.* 23 (2019) 556–565.
- [34] Pengjian Guan, Lin Liu, Xianke Lin, Simulation and experiment on solid electrolyte interphase (SEI) morphology evolution and lithium-ion diffusion, *J. Electrochem. Soc.* 162 (9) (2015) A1798.
- [35] Pengjian Guan, Lin Liu, Yang Gao, Phase-field modeling of solid electrolyte interphase (SEI) cracking in lithium batteries, *ECS Trans.* 85 (13) (2018) 1041.
- [36] Lin Liu, Pengjian Guan, Phase-field modeling of solid electrolyte interphase (SEI) evolution: Considering cracking and dissolution during battery cycling, *ECS Trans.* 89 (1) (2019) 101.
- [37] Zhenliang Mu, Zhipeng Guo, Yuan-Hua Lin, Simulation of 3-D lithium dendritic evolution under multiple electrochemical states: A parallel phase field approach, *Energy Storage Mater.* 30 (2020) 52–58.
- [38] Chih-Hung Chen, Chun-Wei Pao, Phase-field study of dendritic morphology in lithium metal batteries, *J. Power Sources* 484 (2021) 229203.
- [39] Jiawei Zhang, Yuanpeng Liu, Changguo Wang, Huifeng Tan, An electrochemical-mechanical phase field model for lithium dendrite, *J. Electrochem. Soc.* 168 (9) (2021) 090522.
- [40] Yangyang Liu, Xieyu Xu, Matthew Sadd, Olesya O. Kapitanova, Victor A. Krivchenko, Jun Ban, Jialin Wang, Xingxing Jiao, Zhongxiao Song, Jiangxuan Song, Shizhao Xiong, Aleksandar Matic, Insight into the critical role of exchange current density on electrodeposition behavior of lithium metal, *Adv. Sci.* 8 (5) (2021) 2003301.
- [41] Dongge Qiao, Xunliang Liu, Ruifeng Dou, Zhi Wen, Wenning Zhou, Lin Liu, Quantitative analysis of the inhibition effect of rising temperature and pulse charging on lithium dendrite growth, *J. Energy Storage* 49 (2022) 104137.
- [42] Marcos Exequiel Arguello, Monica Gumulya, Jos Derksen, Ranjeet Utikar, Victor Manuel Calo, Phase-field modeling of planar interface electrodeposition in lithium-metal batteries, *J. Energy Storage* 50 (2022) 104627.
- [43] Marcos E. Arguello, Nicolás A. Labanda, Victor M. Calo, Monica Gumulya, Ranjeet Utikar, Jos Derksen, Dendrite formation in rechargeable lithium-metal batteries: Phase-field modeling using open-source finite element library, *J. Energy Storage* 53 (2022) 104892.
- [44] Rui Zhang, Xin Shen, Hao-Tian Ju, Jun-Dong Zhang, Yu-Tong Zhang, Jia-Qi Huang, Driving lithium to deposit inside structured lithium metal anodes: A phase field model, *J. Energy Chem.* 73 (2022) 285–291.
- [45] Yajie Li, Geng Zhang, Bin Chen, Wei Zhao, Liting Sha, Da Wang, Jia Yu, Siqi Shi, Understanding the separator pore size inhibition effect on lithium dendrite via phase-field simulations, *Chin. Chem. Lett.* 33 (6) (2022) 3287–3290.
- [46] Tianyao Ding, In-situ optical microscopic investigation of the dendrite formation on lithium anode under different electrolyte conditions in Li-S battery, 2016.
- [47] Tetsu Tatsuma, Makoto Taguchi, Noboru Oyama, Inhibition effect of covalently cross-linked gel electrolytes on lithium dendrite formation, *Electrochim. Acta* 46 (8) (2001) 1201–1205.
- [48] Oh B. Chae, Jongjung Kim, Brett L. Lucht, Modification of lithium electrodeposition behavior by variation of electrode distance, *J. Power Sources* 532 (2022) 231338.
- [49] William L. George, James A. Warren, A parallel 3D dendritic growth simulator using the phase-field method, *J. Comput. Phys.* 177 (2) (2002) 264–283.
- [50] Keliang Wang, Pucheng Pei, Ze Ma, Huicui Chen, Huachi Xu, Dongfang Chen, Xizhong Wang, Dendrite growth in the recharging process of zinc-air batteries, *J. Mater. Chem. A* 3 (45) (2015) 22648–22655.
- [51] Ryo Kobayashi, Modeling and numerical simulations of dendritic crystal growth, *Physica D* 63 (3) (1993) 410–423.
- [52] Richard Tran, Xiang-Guo Li, Joseph H. Montoya, Donald Winston, Kristin Aslaug Persson, Shyue Ping Ong, Anisotropic work function of elemental crystals, *Surf. Sci.* 687 (2019) 48–55.
- [53] Hui Zheng, Xiang-Guo Li, Richard Tran, Chi Chen, Matthew Horton, Donald Winston, Kristin Aslaug Persson, Shyue Ping Ong, Grain boundary properties of elemental metals, *Acta Mater.* 186 (2020) 40–49.
- [54] Tomohiro Takaki, Takashi Shimokawabe, Munekazu Ohno, Akinori Yamanaka, Takayuki Aoki, Unexpected selection of growing dendrites by very-large-scale phase-field simulation, *J. Cryst. Growth* 382 (2013) 21–25.
- [55] Martin S Alnæs, Jan Blechta, Johan Hake, August Johansson, Benjamin Kehlet, Anders Logg, Chris Richardson, Johannes Ring, Marie E Rognes, Garth N Wells, The FEnics project version 1.5, *Arch. Numer. Softw.* 3 (100) (2015) 9–23.
- [56] Lisandro Dalcin, Yao-Lung L. Fang, Mpi4py: Status update after 12 years of development, *Comput. Sci. Eng.* 23 (4) (2021) 47–54.
- [57] Lisandro D. Dalcin, Rodrigo R. Paz, Pablo A. Kler, Alejandro Cosimo, Parallel distributed computing using python, *Adv. Water Resour.* 34 (9) (2011) 1124–1139, *New Computational Methods and Software Tools*.
- [58] Lisandro Dalcin, Rodrigo Paz, Mario Storti, Jorge D'Elia, MPI for python: Performance improvements and MPI-2 extensions, *J. Parallel Distrib. Comput.* 68 (5) (2008) 655–662.
- [59] Lisandro Dalcin, Rodrigo Paz, Mario Storti, MPI for python, *J. Parallel Distrib. Comput.* 65 (9) (2005) 1108–1115.
- [60] S. Balay, S. Abhyankar, M. Adams, J. Brown, P. Brune, K. Buschelman, L. Dalcin, A. Dener, V. Eijkhout, W. Gropp, D. Karpeyev, D. Kaushik, M. Knepley, D. May, L. Curfman McInnes, R. Mills, T. Munson, K. Rupp, P. Sanan, B. Smith, S. Zampini, H. Zhang, H. Zhang, PETSc users manual, ANL-95/11 - revision 3.15, 2021.
- [61] Charles Monroe, John Newman, Dendrite growth in lithium/polymer systems, *J. Electrochem. Soc.* 150 (10) (2003) A1377.
- [62] L. Vitos, A.V. Ruban, H.L. Skriver, J. Kollár, The surface energy of metals, *Surf. Sci.* 411 (1) (1998) 186–202.
- [63] Richard Tran, Zihan Xu, Balachandran Radhakrishnan, Donald Winston, Wenhao Sun, Kristin A Persson, Shyue Ping Ong, Surface energies of elemental crystals, *Sci. Data* 3 (1) (2016) 1–13.
- [64] Lars Ole Valoen, Jan N. Reimers, Transport properties of LiPF<sub>6</sub>-based Li-ion battery electrolytes, *J. Electrochem. Soc.* 152 (5) (2005) A882.
- [65] W.J. Boettinger, J.A. Warren, C. Beckermann, A. Karma, Phase-field simulation of solidification, *Annu. Rev. Mater. Res.* 32 (1) (2002) 163–194.
- [66] Ken ichi Morigaki, Analysis of the interface between lithium and organic electrolyte solution, *J. Power Sources* 104 (1) (2002) 13–23.
- [67] Bradley Trembacki, Eric Duoss, Geoffrey Oxberry, Michael Stadermann, Jayathi Murthy, Mesoscale electrochemical performance simulation of 3D interpenetrating lithium-ion battery electrodes, *J. Electrochem. Soc.* 166 (6) (2019) A923–A934.
- [68] Utkarsh Ayachit, The Paraview Guide: A Parallel Visualization Application, Kitware, Inc., 2015.
- [69] Brian D. Adams, Jianming Zheng, Xiaodi Ren, Wu Xu, Ji-Guang Zhang, Accurate determination of Coulombic efficiency for lithium metal anodes and lithium metal batteries, *Adv. Energy Mater.* 8 (7) (2018) 1702097.
- [70] Kei Nishikawa, Takeshi Mori, Tetsuo Nishida, Yasuhiro Fukunaka, Michel Rosso, Li dendrite growth and Li<sup>+</sup> ionic mass transfer phenomenon, *J. Electroanal. Soc.* 661 (1) (2011) 84–89.
- [71] Tetsuo Nishida, Kei Nishikawa, M Rosso, Yasuhiro Fukunaka, Optical observation of Li dendrite growth in ionic liquid, *Electrochim. Acta* 100 (2013) 333–341.
- [72] Vladimir Yufit, Farid Tariq, David S. Eastwood, Moshiel Biton, Billy Wu, Peter D. Lee, Nigel P. Brandon, Operando visualization and multi-scale tomography studies of dendrite formation and dissolution in zinc batteries, *Joule* 3 (2) (2019) 485–502.
- [73] Peng Bai, Jinzhao Guo, Miao Wang, Akihiro Kushima, Liang Su, Ju Li, Fikile R. Brushett, Martin Z. Bazant, Interactions between lithium growths and nanoporous ceramic separators, *Joule* 2 (11) (2018) 2434–2449.
- [74] Peng Bai, Ju Li, Fikile R. Brushett, Martin Z. Bazant, Transition of lithium growth mechanisms in liquid electrolytes, *Energy Environ. Sci.* 9 (2016) 3221–3229.
- [75] Rohan Akolkar, Mathematical model of the dendritic growth during lithium electrodeposition, *J. Power Sources* 232 (2013) 23–28.
- [76] Hector Gomez, Thomas J.R. Hughes, Provably unconditionally stable, second-order time-accurate, mixed variational methods for phase-field models, *J. Comput. Phys.* 230 (13) (2011) 5310–5327.
- [77] A.F. Sarmiento, L.F.R. Espath, P. Vignal, L. Dalcin, M. Parsani, V.M. Calo, An energy-stable generalized- $\alpha$  method for the Swift-Hohenberg equation, *J. Comput. Appl. Math.* 344 (2018) 836–851.
- [78] P. Vignal, N. Collier, L. Dalcin, D.L. Brown, V.M. Calo, An energy-stable time-integrator for phase-field models, *Comput. Methods Appl. Mech. Engrg.* 316 (2017) 1179–1214, Special Issue on Isogeometric Analysis: Progress and Challenges.
- [79] Lars-Göran Sundström, Fritz H. Bark, On morphological instability during electrodeposition with a stagnant binary electrolyte, *Electrochim. Acta* 40 (5) (1995) 599–614.
- [80] Guoxing Li, Yue Gao, Xin He, Qingquan Huang, Shuru Chen, Seong H. Kim, Donghai Wang, Organosulfide-plasticized solid-electrolyte interphase layer enables stable lithium metal anodes for long-cycle lithium-sulfur batteries, *Nature Commun.* 8 (1) (2017) 850.
- [81] Jianming Zheng, Mark H. Engelhard, Donghai Mei, Shuhong Jiao, Bryant J. Polzin, Ji-Guang Zhang, Wu Xu, Electrolyte additive enabled fast charging and stable cycling lithium metal batteries, *Nat. Energy* 2 (3) (2017) 17012.
- [82] Jiangfeng Qian, Wesley A. Henderson, Wu Xu, Priyanka Bhattacharya, Mark Engelhard, Oleg Borodin, Ji-Guang Zhang, High rate and stable cycling of lithium metal anode, *Nature Commun.* 6 (1) (2015) 6362.



- [83] Liumin Suo, Yong-Sheng Hu, Hong Li, Michel Armand, Liquan Chen, A new class of solvent-in-salt electrolyte for high-energy rechargeable metallic lithium batteries, *Nature Commun.* 4 (1) (2013) 1481.
- [84] Patrick J. Kim, Kyungho Kim, Vilas G. Pol, Uniform metal-ion flux through interface-modified membrane for highly stable metal batteries, *Electrochim. Acta* 283 (2018) 517–527.
- [85] Xin-Bing Cheng, Ting-Zheng Hou, Rui Zhang, Hong-Jie Peng, Chen-Zi Zhao, Jia-Qi Huang, Qiang Zhang, Dendrite-free lithium deposition induced by uniformly distributed lithium ions for efficient lithium metal batteries, *Adv. Mater.* 28 (15) (2016) 2888–2895.
- [86] Xuelin Yang, Zhaoyin Wen, Xiujian Zhu, Shahua Huang, Electrodeposition of lithium film under dynamic conditions and its application in all-solid-state rechargeable lithium battery, *Solid State Ion.* 176 (11–12) (2005) 1051–1055.
- [87] Aoxuan Wang, Qibo Deng, Lijun Deng, Xuze Guan, Jiayan Luo, Eliminating tip dendrite growth by Lorentz force for stable lithium metal anodes, *Adv. Funct. Mater.* 29 (25) (2019) 1902630.
- [88] Jinwang Tan, Emily M. Ryan, Computational study of electro-convection effects on dendrite growth in batteries, *J. Power Sources* 323 (2016) 67–77.
- [89] Owen Crowther, Alan C. West, Effect of electrolyte composition on lithium dendrite growth, *J. Electrochem. Soc.* 155 (11) (2008) A806.
- [90] A. Wlasenko, F. Soltani, D. Zakopcan, D. Sinton, G.M. Steeves, Diffusion-limited and advection-driven electrodeposition in a microfluidic channel, *Phys. Rev. E* 81 (2010) 021601.
- [91] Guoxing Li, Zhe Liu, Qingquan Huang, Yue Gao, Michael Regula, Daiwei Wang, Long-Qing Chen, Donghai Wang, Stable metal battery anodes enabled by polyethylenimine sponge hosts by way of electrokinetic effects, *Nat. Energy* 3 (12) (2018) 1076–1083.
- [92] Brian D. Iverson, Suresh V. Garimella, Recent advances in microscale pumping technologies: A review and evaluation, *Microfluid. Nanofluid.* 5 (2) (2008) 145–174.
- [93] Mihir N. Parekh, Christopher D. Rahn, Lynden A. Archer, Controlling dendrite growth in lithium metal batteries through forced advection, *J. Power Sources* 452 (2020) 227760.
- [94] X. Wu, G.J. van Zwieten, K.G. van der Zee, Stabilized second-order convex splitting schemes for Cahn–Hilliard models with application to diffuse-interface tumor-growth models, *Int. J. Numer. Methods Biomed. Eng.* 30 (2) (2014) 180–203.
- [95] Andrea Hawkins-Daarud, Kristoffer G van der Zee, J Tinsley Oden, Numerical simulation of a thermodynamically consistent four-species tumor growth model, *Int. J. Numer. Methods Biomed. Eng.* 28 (1) (2012) 3–24.
- [96] Shinji Sakane, Tomohiro Takaki, Takayuki Aoki, Parallel-GPU-accelerated adaptive mesh refinement for three-dimensional phase-field simulation of dendritic growth during solidification of binary alloy, *Mater. Theory* 6 (1) (2022) 1–19.